J. Fluid Mech. (2001), *vol.* 432, *pp.* 127–166. Printed in the United Kingdom

Instability in a viscous flow driven by streamwise vortices

By K. W. BRINCKMAN[1] AND J. D. A. WALKER[2]

[1]PPL Corporation, Allentown, PA 18101, USA

[2]Department of Mechanical Engineering and Mechanics, Lehigh University, 19 Memorial Drive West, Bethlehem, PA 18015, USA

(Received 14 December 1998 and in revised form 10 May 2000)

Unsteady separation processes at large finite, Reynolds number, *Re*, are considered, as well as the possible relation to existing descriptions of boundary-layer separation in the limit $Re \to \infty$. The model problem is a fundamental vortex-driven three-dimensional flow, believed to be relevant to bursting near the wall in a turbulent boundary layer. Bursting is known to be associated with streamwise vortex motion, but the vortex/wall interactions that drive the near-wall flow toward breakdown have not yet been fully identified. Here, a simulation of symmetric counter-rotating vortices is used to assess the influence of sustained pumping action on the development of a viscous wall layer. The calculated solutions describe a three-dimensional flow at finite *Re* that is independent of the streamwise coordinate and consists of a crossflow plane motion, with a developing streamwise flow. The unsteady problem is constructed to mimic a typical cycle in turbulent wall layers and numerical solutions are obtained over a range of *Re*. Recirculating eddies develop rapidly in the near-wall flow, but these eddies are eventually bisected by alleyways which open up from the external flow region to the wall. At sufficiently high *Re*, an oscillation was found to develop in the streamwise vorticity field near the alleyways with a concurrent evolution of a local spiky behaviour in the wall shear. Above a critical value of *Re*, the oscillation grows rapidly in amplitude and eventually penetrates the external flow field, suggesting the onset of an unstable wall-layer breakdown. Local zones of severely retarded streamwise velocity are computed which are reminiscent of the low-speed streaks commonly observed in turbulent boundary layers. A number of other features also bear a resemblance to observed coherent structure in the turbulent wall layer.

1. Introduction

The processes involved in unsteady boundary-layer separation and transition to turbulence in wall-bounded flows have been of considerable interest for some time. An important related process is the regeneration of turbulence in boundary layers through the breakdown of the near-wall flow in the form of strong localized eruptions (see, for example, Smith *et al.* 1991). Despite a wealth of detailed experimental studies over the past several decades, the nature of the physical mechanisms involved in turbulence regeneration remains controversial and several interpretations have been given by Panton (1997). A recurrent theme in the turbulence literature is a suspected presence of counter-rotating streamwise vortices in the near-wall flow, although cause and effect relationships, and even the existence of such vortices, are uncertain. It is known that when counter-rotating vortices are close to a wall at infinite *Re*, the

viscous flow near the surface will break down in a sharply focused eruption (Ersoy & Walker 1986; Herzog & Walker 1988; Smith *et al.* 1991). Here, the main objective is to consider the wall-layer response to the sustained presence of streamwise vortices by consideration of solutions of the Navier–Stokes equations at finite Re; these equations describe the instantaneous flow in the turbulent wall layer when appropriate scaled variables are employed (Walker 1990). In this manner, the high-Reynolds-number limit can be approached systematically from below to ascertain whether other mechanisms of wall-layer breakdown exist. The present results indicate that a vorticity instability occurs at sufficiently high Reynolds numbers in a manner suggestive of the onset of an eruptive state.

A prominent feature of turbulent boundary layers is the persistent presence of 'low-speed streaks' in the near-wall region; these streaks are relatively long zones in the streamwise direction (compared to the spanwise spacing) where the instantaneous streamwise velocity is retarded relative to the local mean (Kline *et al.* 1967; Smith & Metzler 1983). For a majority of any time interval, the low-speed streaks may be observed and the wall layer appears to be passively responding to events taking place in the outer part of the boundary layer. At a certain stage, a streak may become interactive with the outer region via a complex process that is not entirely understood. In such an event, the streak is usually observed to lift away from the wall intermittently and then begin to oscillate before a violent ejection into the outer region occurs, in an event usually referred to as 'bursting'. This ejection appears to be the principal physical mechanism whereby new vorticity from the near-wall region is fed intermittently into the outer region of the boundary layer.

The cause of the low-speed streaks has been controversial, but is believed to be associated with the presence of vortex structures in the turbulence (Head & Bandyopadhyay 1981; Smith *et al.* 1991; Robinson 1991; Smith & Walker 1995). Counter-rotating streamwise vortex pairs can produce streaks, and this model has been a common theme in the turbulence literature (see, for example, Bakewell & Lumley 1967; Blackwelder 1983). Such pairs can transport relatively high-speed fluid toward the wall where it is decelerated and accumulated at the outflow region between the vortices. This low-momentum fluid would eventually be pumped away from the surface and is thought to interact with the high-speed outer flow, to produce a shear layer, as well as the instantaneous inflectional streamwise velocity profile commonly observed in turbulent boundary layers; many authors (see, for example, Stuart 1965) anticipate that this inflectional profile gives rise to a local flow instability leading to bursting. However, there is evidence that an inflectional streamwise profile can evolve without provoking wall-layer instability. Hamilton & Abernathy (1994) suggested that while streamwise vortices will cause inflectional streamwise velocity profiles, only vortices of sufficient strength will lead to wall-layer breakdown. Hall & Horseman (1991), among others, have considered longitudinal vortex motion in a steady boundary layer (and in particular the problem of Görtler vortices on a curved wall) and show that an inflection point is not sufficient for instability in a three-dimensional flow. Thus, the development of inflection points in the streamwise velocity profile is not a general sufficient condition to trigger wall-layer breakdown. The physical mechanism which actually produces instability remains unclear and indeed there may be many routes to breakdown (Hall & Horseman 1991).

The basic vortex element in turbulent boundary layers is undoubtedly more complicated than counter-rotating vortex pairs and is commonly believed to be the hairpin vortex (see, for example, Acarlar & Smith, 1987*a*, *b*; Robinson 1991; Smith *et al.* 1991). Such vortices have a complex three-dimensional shape that distorts as the

vortex is convected in a shear flow near the surface. As discussed by Smith & Walker (1995), hairpin vortices have legs which move downward in the shear flow and become stretched in the streamwise direction; the legs appear, locally at least, to be a counter-rotating vortex pair. In essence, the low-speed streaks are the trails in the wall layer of convecting hairpin vortices near the surface (Smith & Walker 1995). There is good evidence that a hairpin vortex can regenerate itself as it travels downstream over a wall (Robinson 1991; Smith *et al.* 1991; Haidari & Smith 1994; Asai & Nishioka 1995) through a viscous–inviscid interaction with the turbulent wall layer.

The present model is used to investigate the wall-layer response to a persistent streamwise vortex motion at increasing values of Re with the intention of identifying dynamical features in the developing wall layer which may be indicative of the onset of an eruption. It is clear from visualization studies that the viscous flow induced by even a single hairpin vortex is very complex with a rich mixture of lengthscales; this makes good resolution of the associated wall-layer development impractical at high Re owing to computer resource limitations. Thus, a simpler problem is considered which allows solution of the Navier–Stokes equations at relatively high Re, using a sufficiently fine computational grid to resolve intricate details of the developing wall layer adequately under the influence of an array of counter-rotating streamwise vortices, with the motion independent of the streamwise direction. To an extent, this is an approximation of the flow produced by an array of pairs of stretched symmetric hairpin vortex legs. The motion in the streamwise direction, and the initial conditions for the present problem are selected to mimic conditions in a turbulent wall-layer flow during the quiescent period between bursts (Walker *et al.* 1989). The Navier–Stokes equations, in a suitably scaled form, contain a Reynolds number based on the spanwise spacing of the vortices and a velocity characteristic of the strength of the external vortex motion. Numerical solutions were carried out for increasing values of Re for the motion in both the crossflow plane and the streamwise direction. The results indicate that, at a critical Re, instability develops in the streamwise vorticity field, and for sufficiently large Re, this instability grows and eventually corrupts the external flow field. Consequently, the present results suggest another mode of wall-layer breakdown occurring at finite Re, with many features being consistent with observations of turbulent boundary layers.

Another topic related to the present study concerns two-dimensional separation phenomena in general. Much research in this area has been associated with the circular cylinder immersed in a uniform stream. This is the simplest bluff-body problem in two dimensions and with the Reynolds number based on diameter, accurate steady solutions of the Navier–Stokes equations may be obtained with increasing difficulty up to around $Re = 600$ (Fornberg 1985), provided a condition of symmetry across the downstream radius is enforced. At $Re = 7$, a pair of recirculating eddies appears on the rear portion of the cylinder and, with increasing Re, these eddies grow to around 13 cylinder diameters in length at $Re = 600$. This substantial growth in eddy length makes accurate numerical solutions of the symmetric problem very challenging because of difficulties associated with resolving important details in the far wake, where the grid in a conventional cylindrical polar coordinate system becomes quite skewed. The issue of whether a steady limit solution exists for the cylinder has been addressed by a number of authors (see, for example Peregrine 1985; Smith 1985) and the correct structure has been given by Chernyshenko (1988, 1998). The limit solutions describe a very long and thick pair of eddies behind the cylinder.

In principle, the steady limit solution could be approached via a time-dependent integration starting from an impulsive start, and this problem for $Re \to \infty$, has been

considered by a number of authors, most notably Van Dommelen & Shen (1980, 1982). At least the early stages of the boundary-layer development are well understood. A pair of recirculating eddies soon develop near the rear stagnation point in a thin viscous layer. A phenomenon of boundary-layer separation rapidly develops near the upstream edge of the eddies wherein the boundary layer focuses into a narrow eruptive plume that abruptly starts to leave the surface. As shown by Van Dommelen & Shen (1980, 1982), a singularity occurs at this stage, and the spiky, eruptive response at separation is the first time the evolving boundary layer starts to influence the external inviscid flow region. As discussed in Elliott, Cowley & Smith (1983), and Cowley, Van Dommelen & Lam (1990), this viscous response is expected to be generic in two-dimensional boundary layers exposed to an adverse pressure gradient; indeed, similar responses occur in vortex-induced boundary layers (Peridier, Smith & Walker 1991*a*) and for the rotating circular cylinder immersed in a uniform stream (Degani, Walker & Smith 1998). The issue of what happens next, in an expected interaction with the external flow, has not been resolved. Van Dommelen (1981) has speculated that the erupting boundary-layer spikes will roll up into a pair of vortices in an effectively inviscid flow far from the cylinder surface (on the boundary-layer scale). This process might be the first in a sequence of events leading toward the steady asymptotic state described by Chernyshenko (1988), although the precise nature of such events is far from evident. The situation is further complicated by the fact that the first interactive stage contains a high-frequency instability (Cassel, Smith & Walker 1996), and this appears to preclude continuation of the boundary-layer solution into the first stages of interaction.

The present problem is related to the general nature of how the interactions previously discussed take place at high Reynolds numbers. In the limit $Re \to \infty$, the present problem in the crossflow plane is equivalent to the boundary layer on an impulsively started circular cylinder, which is known to terminate in a spiky response. However, for finite *Re*, accurate Navier–Stokes solutions can be found at relatively high values of *Re*, partly because the present vortex-driven problem is not characterized by the enormous normal growth of the recirculating regions that occur for the circular cylinder. An issue of interest here then concerns the range of Reynolds numbers, if any, for which a spiky response starts to evolve in the Navier–Stokes solutions. Spiky eruptions and roll-up into vortex structures have been observed in various experiments (see, for example, Smith *et al.* 1991; Doligalski, Smith & Walker 1994; Smith & Walker 1995), but, thus far, such eruptions have been difficult to compute accurately at high, but finite, Reynolds numbers; the complexity of such events clearly has something to do with this, but the important question remains as to whether or not a smooth transition with increasing Reynolds number can be computed using the Navier–Stokes equations into the spiky boundary-layer eruptions predicted by Van Dommelen (1981) and Elliott *et al.* (1983) (see also Cassel *et al.* 1996). The present results suggest that such a transition is not possible because an instability is encountered in the vorticity field that grows at sufficiently high Reynolds numbers and ultimately spreads to the external flow field. Extensive numerical calculations carried out here suggest strongly that this instability is physical, as opposed to numerical; the onset and characteristics of this instability are documented in some detail.

2. Computational model

The model problem with counter-rotating vortex pairs spaced periodically in the spanwise direction is shown schematically in figure 1. The (y^+, z^+) plane is termed

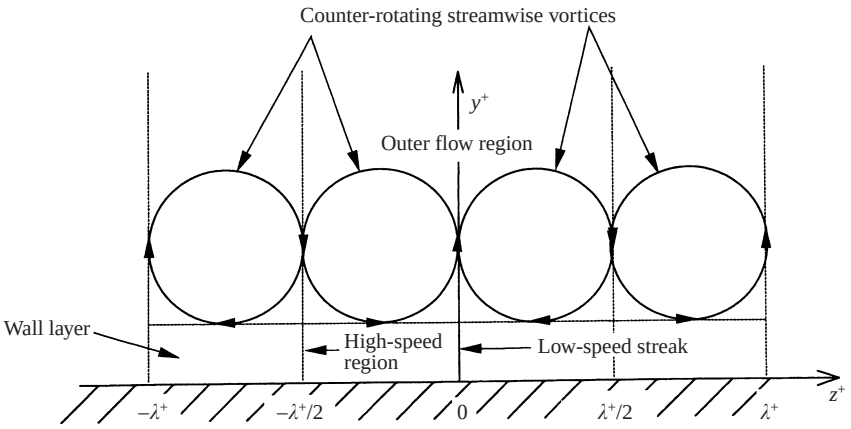

FIGURE 1. Schematic diagram of the assumed wall-layer structure.

the 'crossflow' plane and is normal to the streamwise direction. Scaled coordinates y^+ and z^+ consistent with turbulent wall-layer scalings are

$$y^+ = \frac{yu_\tau}{\nu}, \quad z^+ = \frac{zu_\tau}{\nu}, \tag{1}$$

where u_τ is the local mean friction velocity defined by $u_\tau = (\nu \partial \bar{u}/\partial y)^{1/2}$ evaluated at the wall $y = 0$; here, $\bar{u}$ is the time-mean streamwise velocity and ν is the kinematic velocity. The vortex motion depicted in figure 1 draws high-speed fluid from the outer-flow region towards the wall near $z^+ = \pm\frac{1}{2}\lambda^+$ where it is decelerated to meet the no-slip condition. The counter-rotating motion accumulates low-speed fluid near the upflow planes at $z^+ = 0, \pm\lambda^+$, thereby producing low-speed wall-layer streaks aligned in the streamwise direction similar to those seen in visualization studies of turbulent boundary layers. The streaks are observed to have an average dimensionless spanwise spacing $\lambda^+ = \lambda u_\tau/\nu$ of around 100, where λ is the mean streak spacing (Kline *et al.* 1967; Smith & Metzler 1983). Since the streaks are generally elongated in the streamwise direction with a typical length of the order of 1000 ν/u_τ or more, the scale in the streamwise (x) direction is taken here to be much larger than that in the spanwise and wall-normal directions. The scaled streamwise coordinate is $x^+ = x/L_x$, where L_x is a characteristic length in the x direction such that $L_x \gg \nu/u_\tau$. During a typical quiescent period in the wall layer, when the flow is relatively well-ordered and strong interactions with the outer-flow region do not occur locally, the following scaled velocities are appropriate (Walker *et al.* 1989)

$$u^+ = \frac{u}{u_\tau}, \quad v^+ = \frac{v}{u_\tau}, \quad w^+ = \frac{w}{u_\tau}. \tag{2}$$

These scalings are based on the fact that measured turbulent intensities $\overline{u'^2}, \overline{v'^2}, \overline{w'^2}$ and the Reynolds stress $-\overline{u'v'}$ are generally $O(u_\tau^2)$ in the wall layer (see, for example, Hinze 1975). Substitution of the scalings defined in equations (1) and (2) into the Navier–Stokes equations for incompressible flow yields

$$\frac{\partial u^+}{\partial t^+} + v^+\frac{\partial u^+}{\partial y^+} + w^+\frac{\partial u^+}{\partial z^+} = -p^+ - \frac{\partial p_0}{\partial x^+} + \frac{\partial^2 u^+}{\partial y^{+2}} + \frac{\partial^2 u^+}{\partial z^{+2}}, \tag{3}$$

$$\frac{\partial v^+}{\partial t^+} + v^+\frac{\partial v^+}{\partial y^+} + w^+\frac{\partial v^+}{\partial z^+} = -\frac{\partial p_1}{\partial y^+} + \frac{\partial^2 v^+}{\partial y^{+2}} + \frac{\partial^2 v^+}{\partial z^{+2}}, \tag{4}$$

$$\frac{\partial w^+}{\partial t^+} + v^+\frac{\partial w^+}{\partial y^+} + w^+\frac{\partial w^+}{\partial z^+} = -\frac{\partial p_1}{\partial z^+} + \frac{\partial^2 w^+}{\partial y^{+2}} + \frac{\partial^2 w^+}{\partial z^{+2}}, \tag{5}$$

$$\frac{\partial v^+}{\partial y^+} + \frac{\partial w^+}{\partial z^+} = 0, \tag{6}$$

to leading order, where $t^+ = u_\tau^2 t/\nu$ is the scaled time. Here, the pressure is expanded about the external mainstream pressure $p_\infty(x)$ according to

$$p(x) = p_\infty(x) + pL_x\frac{u_\tau^3}{\nu}p_0(x^+, t^+) + \rho u_\tau^2 p_1(x^+, y^+, z^+, t^+) + \cdots. \tag{7}$$

The pressure term p^+ in equation (3) is the conventional quantity based on the mainstream pressure gradient according to $p^+ = (\nu/\rho u_\tau^3)\,\mathrm{d}p_\infty/\mathrm{d}x$; p^+ is assumed known and normally is small. The variable p_0 is a pressure term which might be impressed across the wall layer by some large-scale disturbance in the outer-layer flow, such as the convected head of a hairpin vortex; a balance of the leading-order terms in the x momentum equation shows that p_0 is a function of x^+ and t^+ at most. Here, p^+ and p_0 are neglected in order to focus on the development of the streamwise velocity due to an assumed streamwise vorticular motion in the outer-flow region. The pressure p_1 is a lower-order term resulting from motion that occurs between streaks during the quiescent state (Walker *et al.* 1989).

Equations (3)–(6) represent the so-called 'two-and-a-half dimensional' form of the Navier–Stokes equations and have been considered previously by Hatziavramidis & Hanratty (1979), Chapman & Kuhn (1986), and Walker & Herzog (1988). These equations may be regarded as approximating a flow that is slowly varying in the streamwise direction. The crossflow plane problem, characterized by equations (4)–(6), decouples from the streamwise velocity problem, but the solution for v^+ and w^+ is then required to solve equation (3) for u^+. The existence of almost uniformly spaced wall-layer streaks aligned in the streamwise direction suggests that the spanwise flow vanishes on planes that, on average, are normal to the wall and parallel to the streamwise direction. The wall-layer development between a typical pair of streaks taken to be located at $z^+ = 0$ and $z^+ = \lambda^+$ (where $w^+ = 0$ for all y^+) is considered here. For symmetric counter-rotating vortices, it is sufficient to study the model problem between symmetry boundaries at $z^+ = 0$ and $z^+ = \frac{1}{2}\lambda^+$. This approach limits the spanwise extent of the problem and permits an efficient use of a computational grid. In the wall-normal direction, the computational problem ranges from $y^+ = 0$ to $y^+ = y_\infty^+$, where y_∞^+ is the location of the computational outer boundary, taken large enough to allow a smooth asymptotic transition of the wall-layer flow to an external flow having the assumed form

$$u^+ \sim \frac{1}{\kappa}\log y^+ + \sum_{n=0}^{\infty}\left\{C_n + \frac{D_n}{y^{+2}} + \cdots\right\}\cos\left(\frac{2n\pi}{y^+}z^+\right), \tag{8}$$

$$v^+ \sim \frac{2\pi}{\lambda^+}W_1 y^+\cos\left(\frac{2\pi}{\lambda^+}z^+\right), \quad w^+ \sim -W_1\sin\left(\frac{2\pi}{\lambda^+}z^+\right), \tag{9}$$

as $y^+ \to \infty$. Equations (9) describe a spanwise periodic flow over a typical cell from $z^+ = 0$ to $z^+ = \lambda^+$ that produces the alternate regions of upflow and downflow at the base of the outer region, as shown in figure 1. Here, W_1 is a constant proportional to the average magnitude of the spanwise velocity near the outer edge of the wall layer during a typical quiescent period and may be thought of as a measure of the strength of the vortices assumed to be residing in the outer flow. The boundary

conditions given by equations (9) satisfy the continuity equation and are therefore asymptotically consistent for large y^+. In equation (8), C_n and D_n are functions of t^+ which can be determined numerically (Brinckman 1996). The boundary condition (8) is selected in order that the streamwise velocity behaves in a manner consistent with measurements which suggest that the instantaneous streamwise profile is logarithmic in the turbulence near the wall; $\kappa = 0.41$ is the von Kármán constant. Note, however, that condition (8) does not affect the crossflow motion, and indeed results similar to those reported here for u^+ were also obtained for external conditions other than (8). Equations (9) represent the simplest outer boundary conditions that will produce the periodic type of motion depicted schematically in figure 1 as $y^+ \to \infty$; in principle, further terms in a Fourier series in equations (9) could be introduced, but this additional complication was not implemented. In the present formulation, the spanwise and wall-normal lengthscales in the wall-layer region are comparable, requiring the solution of the Navier–Stokes equations (3)–(6). It may be noted that Hatziavramidis & Hanratty (1979) and Chapman & Kuhn (1986) have also considered periodic spanwise solutions of equations (3)–(6), but with different external conditions; in the former work, periodic conditions were assumed in time such that the spanwise velocity reversed direction during the course of the integration, whereas, in the latter study, external conditions were introduced from a prior direct numerical simulation of a more complex flow. Note that, in these studies, some of the external conditions imposed were not asymptotically consistent for large y^+ and this is believed to result in various anomalies in their numerical solutions.

Here, the time-invariant condition provided by equations (9) produces a persistent crossflow pumping action over a typical cycle in the wall layer. This model is consistent with the notion of sustained streamwise vortex motion residing above the wall layer during the quiescent period, which impresses a pressure field on the near-wall flow during a period when there is no major viscous–inviscid interaction between the wall-layer and outer-layer regions. The external boundary conditions were allowed to drive the flow in the wall layer until either the numerical solution failed to converge (generally owing to the onset of sharply localized activity), or because an outward-growing wall-layer disturbance started to approach the computational boundary at y_∞^+, thereby suggesting the onset of an interaction. The decoupling of the crossflow and streamwise problems results in a two-dimensional form of the crossflow problem which may be cast in a vorticity-streamfunction formulation with a streamwise vorticity component $\zeta_x^+(y^+, z^+, t^+)$ and streamfunction $\psi^+(y^+, z^+, t^+)$ defined by

$$\zeta_x^+ = \frac{\partial w^+}{\partial y^+} - \frac{\partial v^+}{\partial z^+}, \quad v^+ = -\frac{\partial \psi^+}{\partial z^+}, \quad w^+ = \frac{\partial \psi^+}{\partial y^+}. \tag{10}$$

It is convenient to introduce the following scaled variables

$$Y = \left(\frac{2\pi W_1}{\lambda^+}\right)^{1/2} y^+, \quad V = \left(\frac{\lambda^+}{2\pi W_1}\right)^{1/2} v^+, \quad Z = \frac{2\pi}{\lambda^+} z^+, \quad W = \frac{w^+}{W_1}, \tag{11}$$

$$\Psi = \left(\frac{2\pi}{W_1 \lambda^+}\right)^{1/2} \psi^+, \quad \zeta = \frac{1}{W_1}\left(\frac{\lambda^+}{2\pi W_1}\right)^{1/2} \zeta_x^+. \tag{12}$$

Balancing the time derivative in the streamwise vorticity with the wall-normal diffusion term suggests the following time scaling

$$\tau = \frac{2\pi W_1}{\lambda^+}(t^+ + t_0^+), \tag{13}$$

where t_0^+ is a small parameter which is introduced to accommodate the form of the initial condition that will be discussed subsequently. It is easily shown that the cross-flow problem, (4)–(6), becomes

$$\frac{\partial \zeta}{\partial \tau} + V\frac{\partial \zeta}{\partial Y} + W\frac{\partial \zeta}{\partial Z} = \frac{\partial^2 \zeta}{\partial Y^2} + \frac{1}{Re_\lambda}\frac{\partial^2 \zeta}{\partial Z^2}, \tag{14}$$

$$\frac{\partial^2 \Psi}{\partial Y^2} + \frac{1}{Re_\lambda}\frac{\partial^2 \Psi}{\partial Z^2} = \zeta, \tag{15}$$

while the streamwise momentum equation (3) is

$$\frac{\partial u^+}{\partial \tau} + V\frac{\partial u^+}{\partial Y} + W\frac{\partial u^+}{\partial Z} = \frac{\partial^2 u^+}{\partial Y^2} + \frac{1}{Re_\lambda}\frac{\partial^2 u^+}{\partial Z^2}, \tag{16}$$

where $Re_\lambda = W_1\lambda^+/2\pi$ is the Reynolds number for the problem.

The scaled computational problem extends from $Z = 0$ to π ($z^+ = 0$ to $\frac{1}{2}\lambda^+$) and from $Y = 0$ to some large value of Y. On the symmetry boundaries, relations are applied of the form

$$\Psi = 0, \quad \zeta = 0, \quad \frac{\partial u^+}{\partial Z} = 0 \quad \text{at } Z = 0, \pi, \tag{17}$$

while on the wall

$$\Psi = 0, \quad \frac{\partial \Psi}{\partial Y} = 0, \quad u^+ = 0 \quad \text{at } Y = 0. \tag{18}$$

The asymptotic conditions to be satisfied are

$$\Psi \sim -Y\sin Z + \cdots, \quad \zeta \sim \frac{Y}{Re_\lambda}\sin Z + \cdots \quad \text{as } Y \to \infty. \tag{19}$$

A direct application of the asymptotic form (8) for u^+ gave rise to a problem under certain circumstances on the outflow side of the crossflow plane (near $Z = 0$), where the streamwise velocity became increasingly retarded with time. Here, small oscillations about a well-defined mean eventually occurred (after substantial integration times) between successive vertical mesh points at large Y over a small range of spanwise stations where recirculating flow occurred in the crossflow plane near the wall. Such oscillations persisted when the computational boundary was extended outward substantially, and the mesh was further refined. The origin of this anomaly is not obvious, but appears to be a weak local numerical instability. After considerable effort aimed at alleviating the problem, a compatible derivative boundary condition

$$\frac{\partial u^+}{\partial Y} \sim \frac{1}{\kappa Y} + O\left(\frac{1}{Y^3}\right) \quad \text{as } Y \to \infty, \tag{20}$$

was used. Comparisons of the results produced using the boundary conditions (8) and (20) showed that the streamwise velocity behaviour within the wall layer itself was essentially identical. The only differences were in a small spanwise range near the outer computational boundary where calculations using equation (20) produced a smooth profile consistent with the mean position of the weakly oscillating profile obtained using equation (8).

The initial conditions at $t^+ = 0$ selected in the present study, model a high-speed streamwise flow containing counter-rotating streamwise vortex pairs which penetrate close to the wall at the initiation of the motion; they are selected to mimic a sweep event following a burst. The motion in the crossflow plane at the start of the cycle

$t^+ = 0$ is soon dominated by the abrupt appearance of the counter-rotating motion in the external flow, initiated in an otherwise stagnant crossflow plane motion in the wall layer. Other initial conditions could be assumed (Walker *et al.* 1989), but because of the rapid dominance of the external vortex flow, more elaborate initial conditions were not considered extensively.

For $t^+ > 0$, an unsteady viscous wall layer grows on the surface. For small t^+, the wall layer is very thin and thus the Rayleigh variable χ was introduced, where

$$\chi = \frac{y^+}{2\sqrt{t^+ + t_0^+}} = \frac{Y}{2\sqrt{\tau}}, \tag{21}$$

is $O(1)$ only at locations close to the wall for small t^+. Here, the parameter t_0^+ is introduced so that χ is finite for all y^+ at $t^+ = 0$. Based on considerations of the mean profile for typical turbulent wall-layer flows, Walker *et al.* (1986, 1989) show that t_0^+ must be small and for flow at constant pressure, $t_0^+ = 0.00801$; this value was used throughout the present study. Note that a small value of t_0^+ implies that the logarithmic behaviour in the streamwise profile (8) penetrates close to the wall initially. For $t^+ \gtrsim 0, V$ and W are small, vorticity transport is mainly diffusion away from the wall and equation (14) may be approximated closely by

$$\frac{\partial \zeta}{\partial \tau} = \frac{\partial^2 \zeta}{\partial Y^2}. \tag{22}$$

A solution of equation (22) consistent with the conditions (9) describes the motion in a thin Rayleigh layer having thickness $O(t_0^+)^{1/2}$ as $t^+ \to 0$ and is given by

$$\zeta = \left\{ \frac{Y}{Re_\lambda} - \frac{1}{\sqrt{\pi \tau_0}} \mathrm{e}^{-\chi^2} \right\} \sin(Z), \tag{23}$$

at $t^+ = 0$ (i.e. at $\tau = \tau_0$,where $\tau_0 = 2\pi W_1 t_0^+ / \lambda^+$). Note the external flow is rotational with a weak linear component of vorticity.

The initial condition adopted for the streamwise velocity simulates the wall-layer velocity profile at an instant nearing the end of the sweep event and the onset of the quiescent period. For small t^+, equation (16) is closely approximated by

$$\frac{\partial u^+}{\partial \tau} = \frac{\partial^2 u^+}{\partial Y^2}, \tag{24}$$

and the solution of this equation which satisfies the no-slip condition at the wall and also behaves logarithmically for large y^+according to

$$u^+ \sim \frac{1}{\kappa} \log y^+ + C_i + \cdots, \tag{25}$$

is given by Walker *et al.* (1989) as

$$u^+(Y, Z, \tau_0) = \left\{ \frac{1}{2\kappa} \log(t_0^+) + C_i - \frac{1}{\kappa} \left(\frac{\gamma_0}{2} - \log 2 \right) \right\} \operatorname{erf}(\chi) + \frac{4}{\kappa \sqrt{\pi}} \Xi(\chi), \tag{26}$$

where $\gamma_0 = 0.57721$ is Euler's constant and $\Xi(x)$ is defined as

$$\Xi(\chi) = \int_0^\chi \exp(-\varsigma^2) \int_0^\varsigma \exp(-\alpha^2) \int_0^\alpha \exp(-t^2) \, \mathrm{d}\varsigma \, \mathrm{d}\alpha \, \mathrm{d}t. \tag{27}$$

For various properties of this function, see Walker & Scharnhorst (1986). The constants C_i and κ are often assumed to have universal values of 5.0 and 0.41, respectively,

and for these values, $t_0^+ = 0.00801$. The initial profile (26) is logarithmic almost all the way to the wall at $t^+ = 0$ ($\tau = \tau_0$), except in a thin layer having thickness $O(t_0^{+1/2})$, and simulates the streamwise velocity at the beginning of a local quiescent state. Three-dimensional terms could be added as a Fourier cosine series in Z; this extra complication was not adopted in most of the calculations, since the main interest was to determine the influence of the evolving crossflow plane motion.

3. Numerical solution method

Solutions to the model problem were produced at successively larger values of Re_λ by maintaining $\lambda^+ = 100$ and increasing the characteristic crossflow velocity W_1. Initial calculations were performed using a uniform mesh in the Z-direction. A non-uniform mesh in the normal direction was employed which concentrated points near the wall, and at the same time permitted the computational boundary to be at large Y, thereby facilitating a smooth transition to the asymptotic boundary conditions. As Re_λ was increased, the need for a non-uniform mesh in the spanwise direction became clear. The wall layer began to exhibit intense local spanwise gradients, which developed in zones of recirculation that formed near the surface, especially in the 'alleyways' that ultimately bisected the backflow regions; these alleyways will be described in detail subsequently. From preliminary uniform mesh calculations, a point Z_0 was identified where the spanwise mesh spacing should be decreased in order to resolve the developing severe spanwise variations. A non-uniform (Y, Z) mesh was then produced by mapping the (Z, Y)-plane to a computational (ξ, η)-plane according to the functions

$$\eta = \frac{2}{\pi}\tan^{-1}\left(\frac{Y}{b}\right), \quad \xi = q + \frac{1}{\beta}\sinh^{-1}\left(\left(\frac{Z}{Z_0} - 1\right)\right)\sinh(\beta q), \tag{28}$$

where q is a constant defined by

$$q = \frac{1}{2\beta}\log\left(\frac{1 + (e^{\beta} - 1)Z_0/\pi}{1 + (e^{-\beta} - 1)Z_0/\pi}\right). \tag{29}$$

In computational space, uniform mesh sizes were then used. Here, β and b are parameters which control the spanwise and wall-normal concentration of mesh points in physical space near Z_0 and $Y = 0$, respectively, with larger values of β and smaller values of b implying reduced mesh sizes local to Z_0 and $Y = 0$; as a calculation proceeds, the region of developing spanwise intense variation may shift, and this can be accommodated by stopping the calculation, adjusting the value of Z_0 and then restarting the computation using interpolation. Note that the developing intense spanwise variations are rather different from those encountered in the unsteady separation phenomenon in the limit $Re_\lambda \to \infty$; in the latter situation, a focusing of the viscous flow into a region of zero spanwise thickness eventually occurs, and this behaviour requires the use of Lagrangian techniques to resolve the eruptive behaviour adequately (Van Dommelen 1981; Peridier *et al.* 1991*a*). In the present situation, intense spanwise variations do occur in certain regions of the flow and ultimately lead to the evolution of an instability in the vorticity field. However, severe focusing does not occur, and the flow details can be resolved adequately (with some effort) using an Eulerian formulation with non-uniform mesh transformations.

The governing equations for the model problem were solved numerically over a range of Re_λ using both a finite-difference formulation and a spectral method. In this section, the finite-difference method is described. The governing equations in the

(ξ, η, τ) domain were discretized using a Crank–Nicholson scheme with conventional central difference formulae for second-order spatial derivatives. The first-order spatial derivatives in the convective terms in equations (14) and (16) were approximated by second-order upwind differencing (see, for example, Peridier *et al.* 1991*a*). The method is second-order accurate in both space and time.

The physical location of the outer computational boundary is obtained from equation (28) as $Y_{\max} = b \tan(\frac{1}{2}\pi\eta_{\max})$ and was taken sufficiently large to ensure a smooth asymptotic transition to the outer boundary condition for large Y; to this end, various solutions with different values of $Y_{\max}$ were computed and compared for consistency. The value of $Y_{\max}$ could be decreased as Re_λ was increased because the wall layer becomes thinner at higher Re_λ. The streamfunction–vorticity formulation of the Navier–Stokes equations simplifies the crossflow problem by decoupling the pressure calculation from the solution of the velocity field. However, the problem of specification of the vorticity boundary condition then arises at a solid boundary. In general, it is necessary to construct a method which generates information about the wall vorticity from the available conditions, and many alternative approaches exist in the literature. A number of these were tried in the present study, but the interior constraint method described by Huang (1991) (see also Huang, Modi & Seymour 1995; Huang & Seymour 1995) was found to be particularly effective. A brief summary of the important details is given here for the uniform mesh calculations, and the method for a non-uniform mesh can easily be inferred. Let i and j be mesh point indices in the Z- and Y-directions, respectively. A central-difference approximation to equation (15) at $j = 2$, using the condition $\Psi_{i,1} = 0$ at $Y = 0$ yields

$$\zeta_{i,2} = \frac{\Psi_{i,3} - 2\Psi_{i,2}}{\Delta Y^2} + \frac{1}{Re_\lambda}\frac{\Psi_{i+1,2} - 2\Psi_{i,2} + \Psi_{i-1,2}}{\Delta Z^2}; \tag{30}$$

in effect, this is used as a boundary condition along the line $j = 2$ for the vorticity transport equation (14) in terms of current values of the streamfunction Ψ. The wall vorticity at $j = 1$ was then evaluated from equation (15) using second-order sloping-difference approximations for the Y derivatives and the boundary condition $\Psi_{i,1} = 0$, to yield

$$\zeta_{i,1} = \frac{-5\Psi_{i,2} + 4\Psi_{i,3} - \Psi_{i,4}}{\Delta Y^2}. \tag{31}$$

The derivative boundary condition for Ψ on $Y = 0$ in equation (18) was approximated with a second-order sloping three-point difference and this leads to $4\Psi_{i,2} = \Psi_{i,3}$, which was used in the solution of the difference equations for $\Psi_{i,j}$. Consequently, in the interior-constraint method the difference equations were solved in the domain $j > 2$ with conditions specified on $j = 2$. Boundary conditions on the symmetry boundaries were handled in a conventional manner using central differences.

Finite-difference solutions for the vorticity ζ, streamfunction Ψ, and streamwise velocity u^+ were obtained using a Gauss–Seidel iteration procedure, which was more robust and effective at achieving convergence for higher values of Re_λ than various alternating-direction-implicit methods which were also attempted. Iteration continued at a timestep until the relative changes in the vorticity and streamfunction at each mesh point were less than 10^{-4}. It was found that the use of either under- or over-relaxation had little effect on the convergence rate for the vorticity calculation. In contrast, the streamfunction solution was extremely slow to converge once complex recirculation regions developed in the crossflow plane, and the use of successive-over-relaxation (SOR) proved to be important in obtaining converged results within

practical computational times. For the solution of Poisson's equation in a square region discretized by an $N \times N$ mesh with zero conditions on the boundary, Hockney (1970) gives the over-relaxation factor ω which produces the best asymptotic convergence as the solution approaches zero error as

$$\omega_b = \frac{2}{1 + (1 - \mu^2)^{1/2}}, \quad \mu = \cos(\pi/N). \tag{32}$$

However, using ω_b at the start of an iteration process can produce an error which may initially grow before beginning eventually to decay to zero. A scheme for improving the error decay is referred to by Hockney (1970) as the cyclic Chebyshev method, wherein a variable over-relaxation factor ω is used. In this procedure a point-by-point sweep of the mesh is performed in an odd/even order. First, all the odd points (those for which $(i + j)$ is odd) are corrected and then all the even points are updated in a checker-board type of sweep of the mesh affecting every other point in each half of the iteration process. The cyclic Chebyshev method changes the over-relaxation factor ω every half iteration according to the following scheme (Hockney 1970)

$$\begin{aligned} &\omega^{(0)} = 1, \quad \omega^{(1/2)} = 1/(1 - \tfrac{1}{2}\mu^2), \\ &\omega^{(k+1/2)} = 1/(1 - \tfrac{1}{4}\mu^2\omega^{(k)}) \quad (k = \tfrac{1}{2}, 1, \tfrac{3}{2}, \ldots, \infty). \end{aligned} \tag{33}$$

The first half iteration with $\omega^{(0)}$ is the first sweep of the odd points in the mesh, whereas the second half iteration with $\omega^{(1/2)}$ is the first sweep of the even points; the third half iteration is then the second sweep of the odd points, and so on. The algorithm for ω in equation (33) results in an over-relaxation factor which starts as $\omega = 1$ (Gauss–Seidel) and grows to ω_b as $k \to \infty$. This procedure provided a much improved rate of initial error decay over the standard SOR process and provided stable and rapid convergence for $\Psi_{i,j}$ over a range of Re_λ from 509 to 10^5, even as the crossflow became extremely complicated and rich in recirculation eddies.

The procedure in equation (33) was implemented anew each time the vorticity was updated during a given timestep. At a typical timestep before crossflow recirculation zones develop, the streamfunction solution converged rapidly requiring only a few iterations for each vorticity iteration. As the crossflow streamline patterns became very complicated, the procedure was iterated up to 100 times on the streamfunction equation for several cycles, for each of the vorticity iterations at a given timestep; then a rapid decay to one iteration per vorticity iteration was observed. Experience showed that this method of initially iterating a large number of times on the streamfunction equation before returning to the vorticity iteration was most efficient, although the value selected of 100 iterations is somewhat arbitrary. Once the crossflow problem converged at a given timestep, the streamwise velocity equation was solved using calculated values for the crossflow velocities V and W.

Calculations were performed with a number of mesh sizes and timesteps as a check on accuracy. Typically, 1000 mesh points were eventually used in the spanwise direction along with 400 points in the wall-normal direction. A maximum of 1500 spanwise points was used before computer resource limits were effectively reached. Application of the mesh transformations described in the previous section allowed the mesh to be focused locally by adjusting the values of the parameters b and β in equations (28). The spanwise dimension of the problem was held constant at $z^+ = \frac{1}{2}\lambda^+$ (with a constant $\lambda^+ = 100$). The wall-normal mesh distribution was also influenced by the choice of $y^+_{\max}$, defining the location of the outer boundary. As a calculation proceeds in time, the wall layer thickens owing to viscous diffusion,

Re_λ	β	b	z_0^+	$y_{\max}^+$	$Y_{\max}$
10 000	5	50	12.6	126.5	795
20 000	5	50	12.6	89.4	795
30 000	5	50	12.6	38.8	422
35 000	5	50	12.6	36.0	422
50 000	6	50	14.3	30.0	422
75 000	6	50	15	20	344
∞	3	50	18.7	15.0	211

TABLE 1. Mesh control parameters β, b, z_0^+ and $y_{\max}^+$ (corresponding $Y_{\max}$ shown).

with complex recirculation regions forming in the streamlines near the wall and wall-generated vorticity migrating outward. With increasing Re_λ, it was possible to use smaller values of $y_{\max}^+$ because a thinner and more active wall layer formed and, in addition, the calculation terminated at an earlier elapsed time. The parameters used to define the final mesh for the various Reynolds numbers reported here are given in table 1†. (Note that solutions were produced at other values of Re_λ, but the information in table 1 provides the trend with Reynolds number.) The parameters in table 1 provided a resolution in (y^+, z^+) space of $\Delta y^+ \sim 0.02$ in the near-wall region $y^+ \leqslant 1$, and $\Delta z^+ \sim 0.02$ in the region $z_0^+ \pm 2$. A maximum mesh spacing of $\Delta z^+ \sim 0.23$ occurred at $z^+ = \frac{1}{2}\lambda^+$, while the maximum Δy^+ value used in the region $y^+ \leqslant 10$ was 0.1.

4. Spectral solution

The solutions of the model problem were found to be unexpectedly complex, especially at high Re_λ, and in order to provide an independent check on the finite-difference results, the model problem was also solved using a spectral method. The details are similar to that in Ece, Walker & Doligalski (1984) and can be found in Brinckman (1996). During a typical calculation, the vorticity and crossflow streamfunction were expanded according to

$$\zeta = \frac{2\sqrt{\tau}\chi}{Re_\lambda} \sin Z - \frac{1}{2\sqrt{\tau}} \sum_{n=1}^{\infty} \tilde{G}_n(\chi, \tau) \sin(nZ), \tag{34}$$

and

$$\Psi = -2\sqrt{\tau}\chi \sin Z - 2\sqrt{\tau} \sum_{n=1}^{\infty} \tilde{F}_n(\chi, \tau) \sin(nZ), \tag{35}$$

in terms of the variable Z and the Rayleigh variable χ, defined in equation (21). The expansion for the streamwise velocity is

$$u^+ = u_0(\chi, \tau) + \sum_{n=1}^{\infty} u_n(\chi, \tau) \cos nZ. \tag{36}$$

† A referee has suggested that in order for the limit problem as $Re_\lambda \to \infty$ to be the same as for the impulsively started circular cylinder, the value of $Y_{\max}$ should have been selected so that $Y_{\max}$ varies explicitly as $Re_\lambda^{-1/2}$. It may be confirmed that the values quoted in table 1 conform roughly to this trend. Note, however, that different values of $Y_{\max}$ were considered for each Re_λ, and the results are believed to be independent of $Y_{\max}$.

Here, $\tilde{G}_n$, $\tilde{F}_n$, u_o and u_n are functional coefficients satisfying a coupled set of partial differential equations obtained by substitution of the expansions (34)–(36) into equations (14)–(16), and use of standard methods for orthogonal functions.

Numerical solutions for $\tilde{G}_n$, $\tilde{F}_n$ and u_n were obtained for various Reynolds numbers. In general, each series must be truncated at some value of $n = N$. As the crossflow solution became increasingly complex, an increasing number of Fourier terms N was required to resolve the flow field, particularly for the vorticity solution. Generally, fewer than 30 terms were needed to resolve the crossflow solution at early times, before the solution began to develop appreciable spanwise gradients. At any timestep, N coupled tri-diagonal matrix problems must be solved; the spectral method was very efficient as long as the flow field was relatively smooth and N could be taken as less than 100. At each timestep a check on the Nth mode of the vorticity coefficient at the wall was made to ensure that the number of terms used was large enough to maintain the value of $\tilde{G}_N$ several orders of magnitude less than the leading-order term $\tilde{G}_1$, corresponding to the first term in the sum on the right-hand side of equation (34). This provided a sufficiently well-converged series solution such that additional terms yielded no apparent increase in the resolution of the flow field. In the terminal stage of some of the calculations, as many as 800 terms were required to resolve the complex patterns in the crossflow field; at this stage, the spectral method was far less efficient than the finite-difference method, and the spectral method had to be abandoned. For this reason, it was generally not feasible to continue the integration all the way to the breakdown times using the spectral method.

The number of Fourier modes used in the streamwise problem was, in general, less than the number N used for the crossflow problem. Similar to the crossflow problem, the number of Fourier terms used in the streamwise problem was increased as the flow became increasingly complex. A check was made at each timestep and, generally, a maximum of 100 to 200 modes for the streamwise problem was required in the terminal stages of a solution.

5. Results

Numerical solutions to both the crossflow and streamwise problems were obtained for a range of Reynolds numbers from $Re_\lambda = 509$ to 10^5. Experiments suggest λ^+ is a constant over a wide range of Reynolds numbers and $Re_\lambda = W_1\lambda^+/2\pi$ was increased by maintaining $\lambda^+ = 100$ corresponding to the average streak-spacing, and increasing W_1. A number of timesteps were used as a check on the accuracy. Typically, the solutions were advanced in time using a timestep $\Delta\tau = 0.001$ for all Reynolds numbers; this value provided rapid convergence and halving the timestep size produced no perceivable change in the solutions. Results are presented with respect to the scaled time τ defined by equation (13) and the conventional turbulence variables defined by equation (1). The scaled time τ is non-zero at $t^+ = 0$, and as the value of W_1 is increased, the initial time τ_0, corresponding to $t^+ = 0$, also increases. To allow a consistent comparison between various Reynolds numbers, calculated results are presented in terms of an elapsed time τ_e, defined as $\tau_e = \tau - \tau_0$. The subscript is dropped for simplicity and all subsequent figures and discussions use the symbol τ to represent elapsed time.

Increasing values of W_1 imply a stronger vorticular motion in the external flow. The limit problem $Re_\lambda \to \infty$ in the crossflow plane motion is identical to that for the boundary layer on an impulsively started circular cylinder, for which the surface layer is known to erupt in a spiky manner at $\tau \approx 3$ indicating the onset of interaction (Van

Dommelen & Shen 1980, 1982). The present results show that the adverse spanwise pressure gradient imposed near the wall by the outer flow always induces a pair of recirculating regions, which are symmetric about $z^+ = 0$ and are analogous to eddies behind a circular cylinder in a uniform stream. The development following the onset of crossflow separation is highly dependent on the Reynolds number. Solutions of the problem have previously been obtained by Walker & Herzog (1988) for $Re_\lambda = 509$ and the limit problem ($Re_\lambda \to \infty$) using a spectral approach. For $Re_\lambda = 509$, the crossflow solution approaches an apparently steady state, while the streamwise velocity profiles continue to evolve, eventually exhibiting an inflectional behaviour; these solutions were closely reproduced using the present finite-difference formulation, and solutions were then obtained for a number of larger values of Re_λ. Detailed computational results are given by Brinckman (1996) and here only an abbreviated summary is given. A main conclusion is that above a certain Reynolds number, an instability occurs in the crossflow plane motion, which is characterized by the formation of high-frequency oscillations in the streamwise vorticity field at certain specific locations. In fact, it is possible to classify the motion into four Reynolds number ranges based on the calculated crossflow behaviour; these ranges are as follows: (i) a 'steady' range for $Re_\lambda < 5000$ where the crossflow motion ultimately evolves toward a steady state; (ii) a 'stable' range for $5000 \leqslant Re_\lambda \leqslant 20\,000$ where the crossflow and streamwise velocity solutions continue to develop with time, but the solution does not exhibit a tendency towards either an instability or a local eruption; (iii) a 'transitional' range for $20\,000 \leqslant Re_\lambda \leqslant 35\,000$, where spanwise high-frequency oscillations in the streamwise vorticity contours occur near certain alleyways associated with bifurcating recirculation zones; in this range, the oscillations are eventually convected away from their point of origin and do not grow or affect the external flow; and (iv) an 'unstable' range for $Re_\lambda > 35\,000$ wherein the vorticity oscillations appear in the wall layer, grow rapidly with time and eventually penetrate and corrupt the external flow. Note that because each calculation could require several weeks to complete on a workstation, the Reynolds number ranges quoted here are only approximate.

The process leading to the formation of oscillations in the streamwise vorticity is very complicated, and it is useful to show first the critical stages in development schematically. Figure 2 shows important elements in development of the vorticity field along with companion schematics of the crossflow motion. The structure of the flow field can be conveniently characterized in the two-dimensional crossflow plane by plotting the boundaries of recirculating eddies for the streamlines and the zero vorticity lines. The contours plotted are from an actual calculation for $Re_\lambda = 50\,000$ and are presented with a minimum of detail to clarify the physical mechanisms involved. For informational purposes, the elapsed times for the $Re_\lambda = 50\,000$ calculation are quoted, but the development in figure 2 should be regarded as characteristic over a range of Re_λ.

At early times, a thin layer of negative vorticity forms along the wall and diffuses outward toward the positive vorticity in the outer flow. The adverse-pressure gradient imposed on the wall by the external motion induces the evolution of a 'primary' recirculating eddy at the wall, as shown in figure 2(*a*); this is accompanied by the formation of a corresponding region of positive streamwise vorticity, as shown in figure 2(*b*). For sufficiently high Re_λ, the primary eddy is observed to bifurcate into multiple eddies through formation of a secondary eddy as shown in figure 2(*c*) near $z^+ = 15$. The secondary eddy forms at the wall under the influence of the local adverse pressure gradient due to a portion of the primary eddy in much the same way as described by Peridier *et al.* (1991*a*). The secondary eddy grows in a direction normal

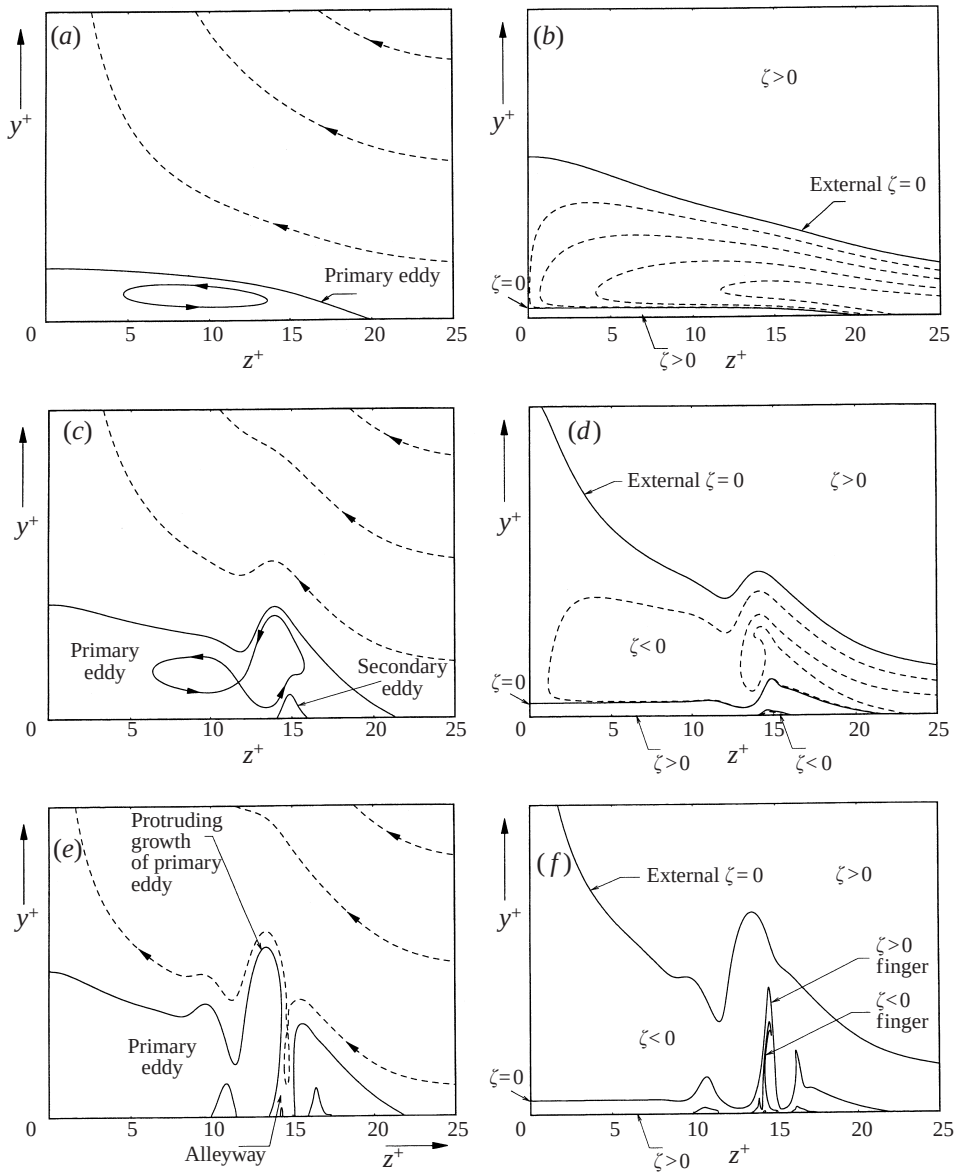

FIGURE 2 (*a–f*). For caption see facing page.

to the wall and eventually splits the primary eddy to form what will be referred to as an 'alleyway' in figure 2(*e*). The flow within the narrow alleyway is primarily in the normal direction, both up and down, but generally contains a small eddy. At the base of the alleyway, values of the wall shear tend to develop a sharp negative minimum. The strong updrafts in the alleyway convect local regions of wall-generated vorticity outward in the form of almost spike-like fingers, as shown in the streamwise vorticity contours in figure 2(*f*). Note in figure 2(*e*) that the primary eddy starts to develop an outward growth in the form of a thick protruding finger, at about the same spanwise location as the limit solution $Re_\lambda \to \infty$ eventually forms an eruptive spike (Walker & Herzog 1988). The finger might be regarded as the analogue of the

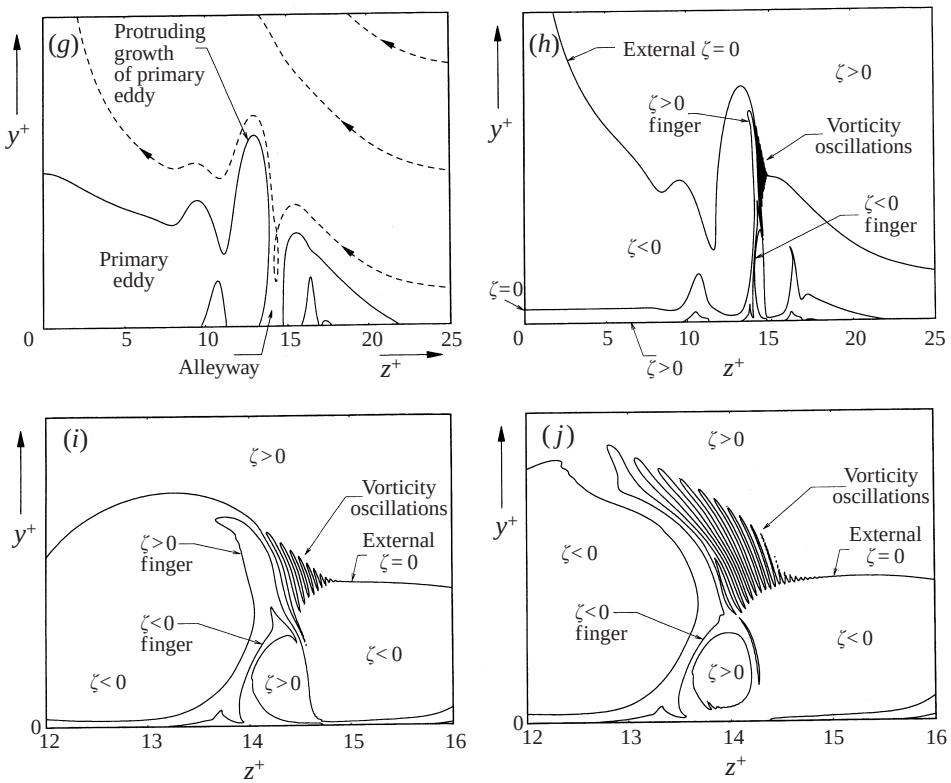

FIGURE 2. (a, b) Schematic of the wall-layer in the crossflow plane following formation of the primary recirculating eddy ($\tau = 1.78$). (a) Crossflow streamlines; (b) streamwise vorticity. (c, d) Schematic of the wall-layer development in the crossflow plane following formation of the secondary recirculating eddy ($\tau = 2.40$). (c) Crossflow streamlines; (d) streamwise vorticity. (e, f) Schematic of the wall-layer development in the crossflow plane following alleyway formation in the primary eddy ($\tau = 2.76$). (e) Crossflow streamlines; (f) streamwise vorticity showing growth of vorticity fingers from the wall. (g, h) Schematic of the wall-layer development in the crossflow plane following the onset of instability ($\tau = 2.86$). (g) Crossflow streamlines; (h) streamwise vorticity with oscillations in the zero-vorticity contour. (i) Streamwise vorticity contours in the crossflow plane; magnified view of the oscillations in (h). (j) Local streamwise vorticity contours in the cross-flow plane for a Reynolds number in the unstable range ($\tau = 2.96$).

limit solution separation spike, but having finite thickness at finite Re_λ; indeed, in an effort to verify this, calculations were run up to $Re_\lambda = 10^5$ (with increasing difficulty), and a progressive decrease in width of the protruding finger shown in figure 2(e) was observed. The formation of the alleyway is a new feature, however, which is not observed in the boundary-layer solution (Walker & Herzog 1988).

In the stable range ($Re_\lambda < 20\,000$), alleyways were observed to form in the primary eddy and then subsequently close up without any evidence of significant interaction with the external flow. On the other hand, in the transitional range and above ($Re_\lambda > 20\,000$), where vorticity oscillations were observed, the alleyway in the streamline patterns is sustained such that the vorticity 'fingers' continue to move outward from the wall. As the positive-vorticity finger nears interaction with the positive vorticity of the outer flow, high-frequency oscillations develop in the local zero-vorticity contour, as illustrated in figure 2(h). A close-up of the evolution of the vorticity fingers just following the onset of the instability is shown in figure 2(i) for the situation depicted

in figure 2(*h*). As illustrated in figure 2(*i*), the oscillations become prominent just before the positive-vorticity finger merges with the positive vorticity of the outer flow; eventually, a merger occurs as shown in figure 2(*j*). The onset of the oscillations was always preceded by the development of a local absolute negative minimum in wall shear in a narrow spanwise band centred on the alleyway; with the appearance of the oscillations, this minimum in wall shear relaxes and is dramatically reduced. For $Re_\lambda \geqslant 35\,000$, the process appears strong enough to drive the disturbance ultimately all the way into the outer flow. In general, the oscillations appear to persist as long as the alleyway in the primary eddy remains open. In the transitional range and above, the phenomenon of an alleyway and fingers of wall-generated vorticity protruding outward to produce oscillations in the streamwise vorticity was observed to repeat itself at various spanwise locations, thereby potentially giving rise to multiple breakdown sites.

For $Re_\lambda < 20\,000$, the wall layer evolved with the same basic crossflow characteristics shown schematically in figure 2, with the exception that the interaction of the outer-flow within the alleyway does not appear to be strong enough to drive the same instability observed for $Re_\lambda \geqslant 20\,000$. For example, figure 3 shows the crossflow development at $Re_\lambda = 10\,000$. The general structure of any two-dimensional flow can be deduced by plotting the boundaries of recirculation zones ($\Psi = 0$ contours) and critical points either at an eddy centre (shown in figure 3 as a dot) or on the eddy boundaries; this is done in figure 3 to provide only the essential details and the general paths of additional streamlines can easily be inferred. At $\tau = 3.95$, figure 3(*a*) shows a prominent alleyway in the crossflow streamlines, along with the development of the characteristic vorticity finger protruding from the wall at $z^+ \approx 11.5$ in figure 3(*b*). At $\tau = 4.75$, a second alleyway is about to open up near $z^+ \simeq 16$ as shown in figure 3(*c*), but notice that the primary (first) alleyway has now closed. The vorticity finger, corresponding to the primary alleyway, which is still prominent in figure 3(*d*), begins to subside at later time and never grows to penetrate with the external flow region. Finally, at $\tau = 9.1$, figure 3(*e*) shows a crossflow structure which is rich in wall-layer eddies but lacking a prominent alleyway to permit a strong local interaction with the outer flow. As a result, the corresponding zero-vorticity contours in figure 3(*f*) do not possess the prominent spiking shown schematically in figure 2(*f*), which lead to the vorticity oscillations observed at higher Reynolds numbers.

The opening and closing of the alleyways, as well as the cascade to progressively smaller eddy structures near the wall, was to some extent unexpected, and considerable effort was made to ensure that the observed phenomena were physical and not associated with numerical error. Additional support for such behaviour is available in the work of Loc & Bouard (1985), who have computed the initial flow past a circular cylinder at high Reynolds number using the Navier–Stokes equations, for a flow which is symmetric about the downstream radius. Their results compare well with experimental flow visualization studies of Bouard & Coutanceau (1980) and predict the formation of a strong secondary eddy inside a primary eddy attached to the cylinder surface. At high Reynolds number, the secondary eddy was observed to grow and split the primary eddy; with the passage of time, multiple secondary eddies formed within the primary recirculation zone which split and reclosed in an evolution where, according to Loc & Bouard (1985), 'the secondary vortices interact alternatively with the external flow and the main wake'. In fact, the results of Loc & Bouard (1985) at their Reynolds number of 9500 are strikingly similar to the present results at $Re_\lambda = 10\,000$. Loc & Bouard (1985) also report local 'peaks of vorticity' at the wall which are associated with the presence of the secondary eddies above; the

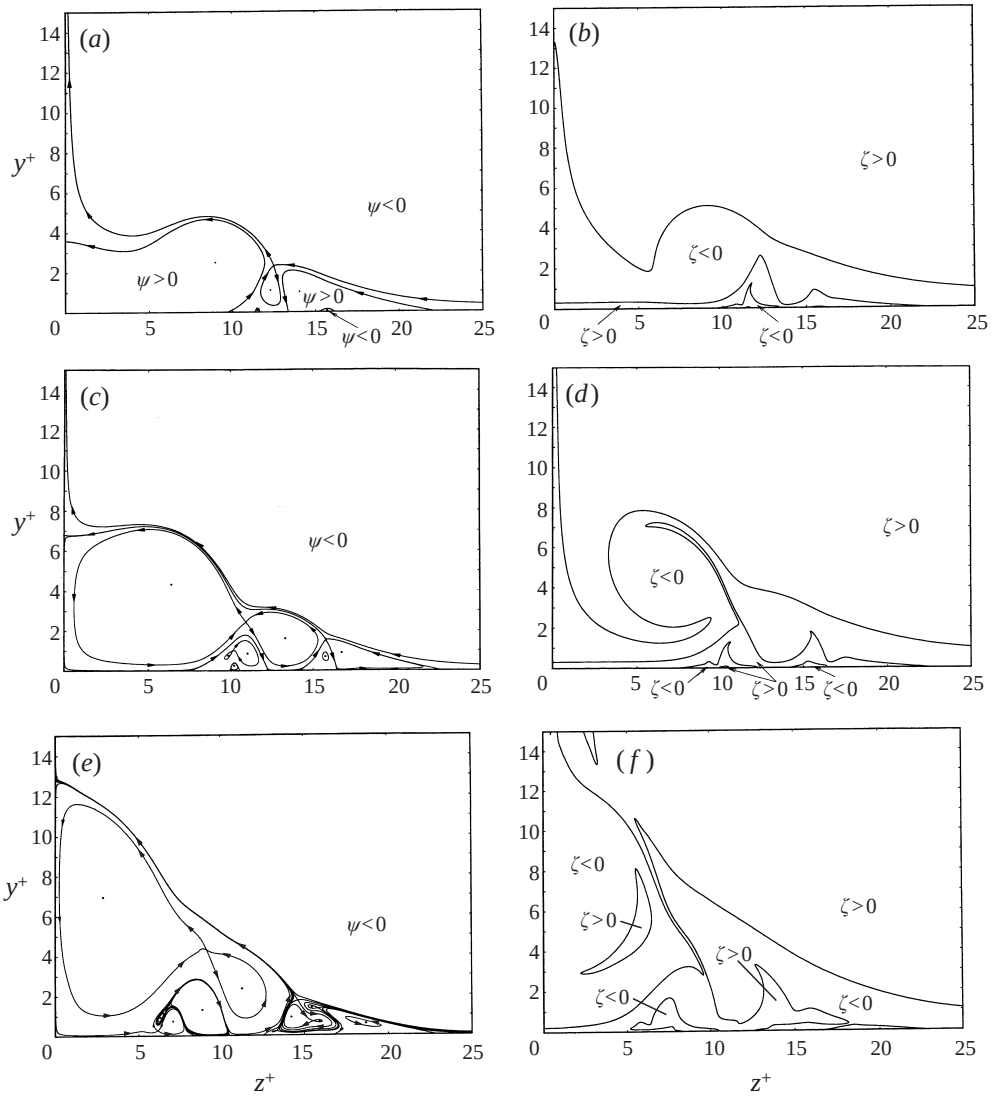

FIGURE 3. (a, b) Crossflow solution for $Re_\lambda = 10\,000$ at $\tau = 3.95$. (c, d) Crossflow solution for $Re_\lambda = 10\,000$ at $\tau = 4.75$. (e, f) Crossflow solution for $Re_\lambda = 10\,000$ at $\tau = 9.1$. (a, c, e) Instantaneous streamlines; (b, d, f) contours of streamwise vorticity $\zeta = 0$.

magnitude of these peaks, generally, was observed to increase with Reynolds number, which is consistent with the present results for the crossflow shear. Additionally, in the two-dimensional unsteady Navier–Stokes solutions for a driven cavity flow carried out by Shen (1991), recirculating corner eddies were found to develop over a range of Reynolds numbers. Shen (1991) classified the behaviour into three categories. The solutions at low Reynolds numbers were found to converge to a steady state, while in an intermediate range of Re; the flow became periodic in time. Above a critical Re, the solutions lost periodicity and did not converge to a steady state. Results at a Reynolds number in the intermediate range predicted the formation of a secondary eddy below the primary eddy. This secondary eddy formed and subsided periodically with time. At higher Reynolds numbers, Shen (1991) reports that corner eddies split

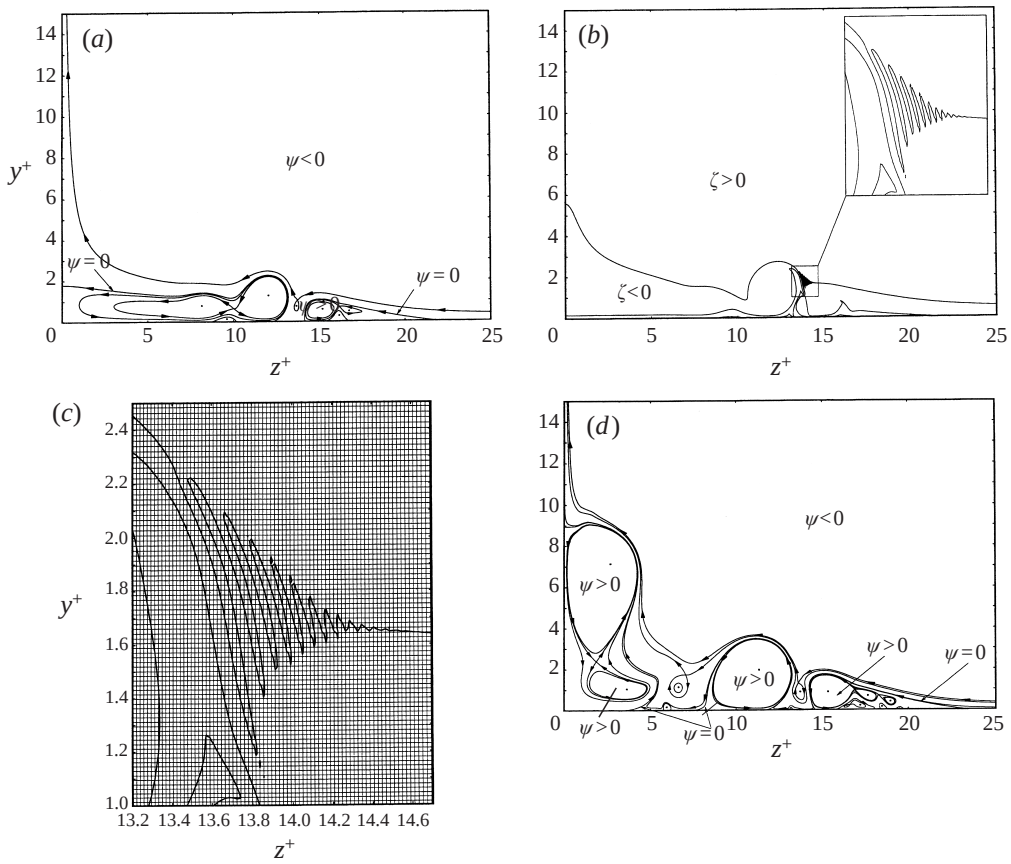

FIGURE 4 (*a–d*). For caption see facing page.

into two separate vortices, and the resulting alleyway was sustained for a period of time before the eddies coalesced. At the higher Reynolds numbers investigated in the present study, the complexity of the eddy structure increased with Reynolds number as eddies bifurcated and rejoined without evolving to a steady state in a behaviour consistent with the results of Shen (1991). Recently, similar behaviour has been observed in Navier–Stokes solutions for a thick-core vortex convected above a plane wall (Obako & Cassel 2000).

In the present transitional range ($20\,000 \leqslant Re_\lambda < 35\,000$), once an alleyway to the wall opens up, oscillations in the vorticity field occur eventually above the alleyway. The transitional range is characterized by the fact that the oscillations are convected away, toward $z^+ = 0$, and by and large do not increase in the process or penetrate toward the outer region. A typical case at the upper end of the transitional range is shown in figure 4 for $Re_\lambda = 35\,000$. Figures 4(*a*) and 4(*b*) show the streamlines and streamwise zero-vorticity contours at $\tau = 3.08$, just after the onset of the instability. Notice the prominent alleyway which produces the vorticity finger at $z^+ \approx 13.5$. The local grid is superimposed over the vorticity oscillations in figure 4(*c*) to show that the instability can be adequately resolved on the present numerical mesh. Subsequently, at $\tau = 5.11$, a second alleyway has developed and a second site of vorticity oscillations at $z^+ \approx 14$ has been triggered, as shown in figures 4(*d*) and 4(*e*). Note that the initial alleyway and associated vorticity oscillations have moved to near $z^+ = 6$. As

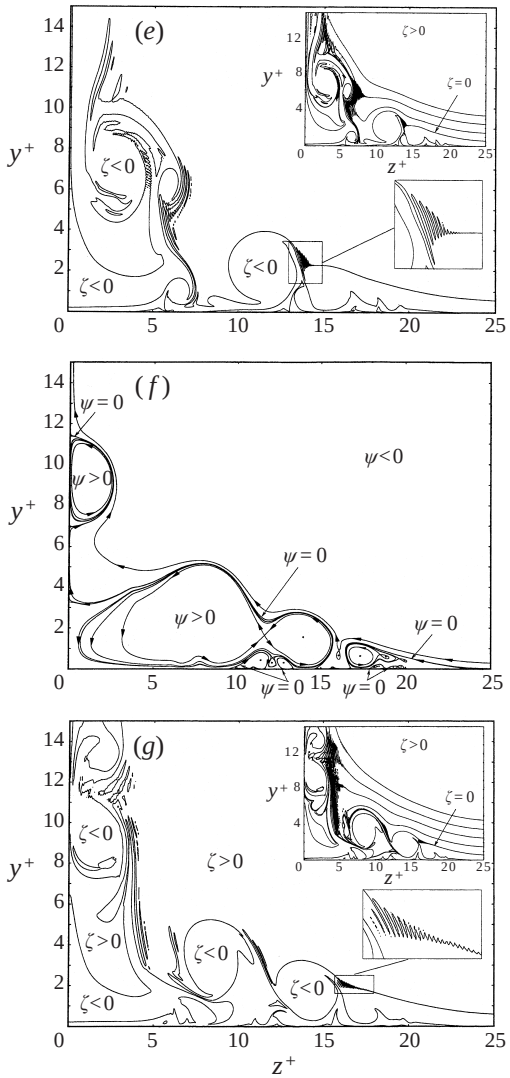

FIGURE 4. (*a*, *b*) Crossflow solution for $Re_\lambda = 35\,000$ at $\tau = 3.08$. (*a*) Instantaneous streamlines; (*b*) contours of streamwise vorticity $\zeta = 0$; magnified view of oscillations shown in window. (*c*) Vorticity oscillations superimposed over the finite-difference mesh. (*d*, *e*) Crossflow solution for $Re_\lambda = 35\,000$ at $\tau = 5.11$. (*d*) Instantaneous streamlines; (*e*) contours of streamwise vorticity $\zeta = 0$; additional contours of positive vorticity local to instability shown in upper window. (*f*, *g*) Crossflow solution for $Re_\lambda = 35\,000$ at $\tau = 5.8$. (*f*) Instantaneous streamlines; (*g*) contours of streamwise vorticity $\zeta = 0$; additional contours of positive vorticity local to instability shown in upper window.

the crossflow motion develops further, figures 4(*f*) and 4(*g*) show a third alleyway which has formed at $\tau = 5.8$ leading to a third instability near $z^+ \approx 15.5$. At the same time, a fourth site appears to be developing near $z^+ = 18$. Additional vorticity contours in the outer-flow region are plotted in the window of figures 4(*e*) and 4(*g*) to illustrate the outward propagation of the instability; these contours of positive vorticity in the outer-flow region have developed an oscillatory behaviour apparently due to the disturbance from the wall-layer instability as it has continued to grow outward with time. This case is approximately the upper limit of the transitional

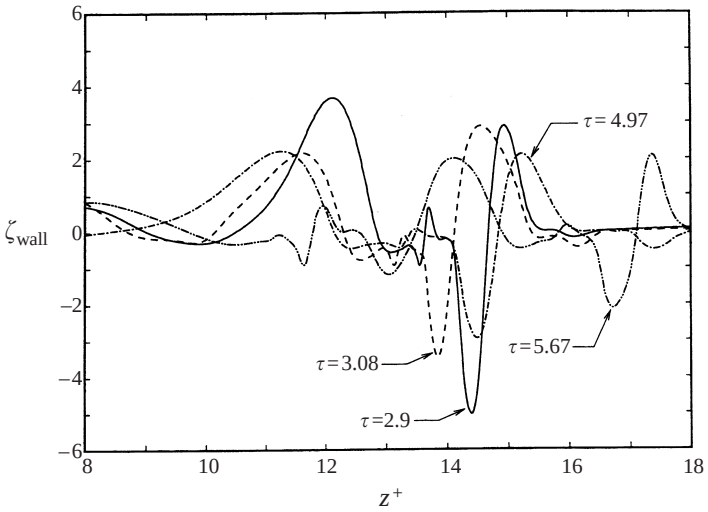

FIGURE 5. Temporal development of wall vorticity for $Re_\lambda = 35\,000$.

regime and for cases with $Re_\lambda < 35\,000$, the oscillations tend to be convected away from the alleyway in which they were born and then apparently damped out. A strong effect on the outer-region vorticity is only predicted for $Re_\lambda \geqslant 35\,000$ and a breakdown occurs at earlier times as the Reynolds number is increased. Figure 5 shows the temporal development of the dimensionless cross-stream wall shear ($\partial w^+/\partial y^+$) for $Re_\lambda = 35\,000$, and depicts the local peaks in negative wall shear which occur at the spanwise location of the alleyway, reaching an absolute minimum just prior to the onset of oscillations in the streamwise vorticity contours; with the onset of the vorticity oscillations, the peak relaxes significantly. The peak in wall shear at $\tau = 2.9$ corresponding to the first alleyway is clearly of the largest magnitude, and this value consistently increases with an increase in Reynolds number. Note the dip in wall shear at $\tau = 4.97$ near $z^+ = 14.5$, which precedes the onset of the oscillation shown in figure 4(*e*), is associated with the opening of the second alleyway. A similar event occurs with a negative peak at $\tau = 5.67$ near $z^+ = 16.5$ in figure 5, and this heralds the evolution of an instability associated with the third alleyway that is evident in figure 4(*g*). These wall shear peaks provided a reliable precursor to the onset of vorticity oscillations for all Reynolds numbers where the instability occurred. Lastly, consider a case well within the unstable regime; in figure 6 vorticity contours near the terminal stages of a calculation for $Re_\lambda = 50\,000$ are shown at $\tau = 4.54$. A comparison with figure 4(*g*) illustrates how the wall-layer instability grows and interacts more prominently with the external flow at an earlier time. In such cases, the calculations were terminated once the instability approached the upper computational boundary.

For the streamwise problem, streamwise velocity profiles were plotted along with surface contours of the streamwise velocity, the latter being a three-dimensional plot of the magnitude of streamwise velocity over the extent of the crossflow plane. In essence, the surface plot consists of an infinite number of adjacent u^+ profiles across the span, thereby providing a complete picture of the streamwise velocity. Individual profiles are also plotted at various spanwise locations in order to reveal the potential presence of inflection points in the streamwise profiles; such points suggest that the motion might be inviscidly unstable to small disturbances. Walker & Herzog (1988) noted the development of a strong inflectional behaviour in the streamwise velocity

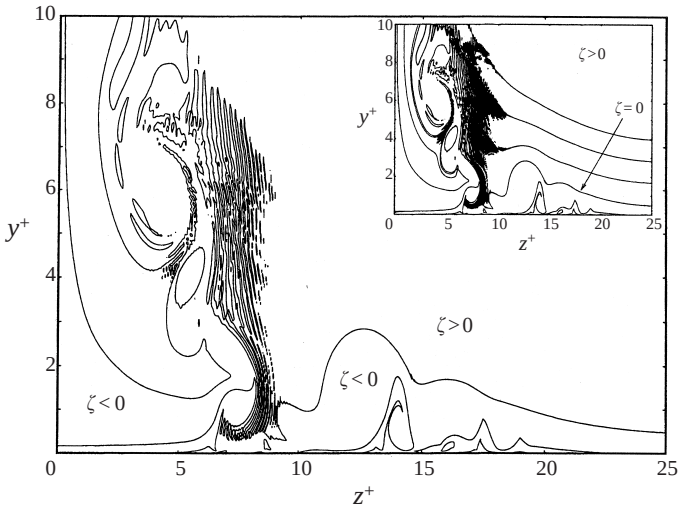

FIGURE 6. Contours of streamwise vorticity $\zeta = 0$ for $Re_\lambda = 50\,000$ at $\tau = 4.54$; additional contours of positive vorticity local to instability shown in window.

profiles at low Reynolds numbers ($Re_\lambda = 509$). Figure 7 illustrates the development for $Re_\lambda = 10\,000$ for a select sequence of times. In figures 7(*a*)–7(*d*), results are plotted to $y^+ \leqslant 15$, but the scale of figures 7(*g*) and 7(*h*) is expanded to $y^+ = 30$ to accommodate the fact that the outward flow near $z^+ = 0$ continuously convects deformations in the streamwise velocity profiles towards the outer boundary. Figures 7(*a*) and 7(*b*) show results for the streamwise velocity at the early time $\tau = 1.0$. Near the outer boundary, the outer flow sweeps across the crossflow plane toward $z^+ = 0$; fluid with high-speed streamwise velocity is brought in near $z^+ = 50$, and the streamwise velocity of the fluid leaving the domain between $z^+ = 0$ and $z^+ = 25$ is progressively reduced. As time continues, the streamwise velocity profiles at spanwise locations of $z^+ < 30$ exhibit varying degrees of inflectional behaviour and dimples form in the surface contour. This behaviour is directly associated with the zones of recirculation that form in the crossflow plane as illustrated in figures 7(*c*) and 7(*d*); in figure 7(*c*), the boundaries of the recirculating eddies are superimposed on the streamwise velocity contour. The profiles are strongly inflectional when under the influence of the developing crossflow recirculating eddies. It appears that the fluid trapped within the eddies is continuously recirculated past the wall where it is decelerated. The transition back and forth between high and low speed within the eddies gives rise to the inflectional behaviour in the streamwise velocity profiles. The streamwise motion above the eddies retains the basic logarithmic profile of a turbulent boundary-layer flow, but it is worthwhile to note that the particular boundary condition for the streamwise profile at y_∞^+ has little effect on the development near the wall, and external conditions other than (8) produce similar results to those obtained here. Note that the profiles at $z^+ = 30$–50, never exhibit an inflectional behaviour, as the crossflow recirculation is confined to $z^+ < 25$, and does not influence the streamwise motion at $z^+ \geqslant 30$. The temporal development of the surface contours provides revealing insight into the evolution of the streamwise velocity. Figure 7(*e*) shows the continued development of a local deficit or 'dimple' in the streamwise velocity surface corresponding to the location of the primary eddy at $\tau = 3.95$. As time increases, the dimple in the surface contour grows and becomes increasingly prominent. By $\tau = 9.1$, the primary crossflow eddy begins to thin and

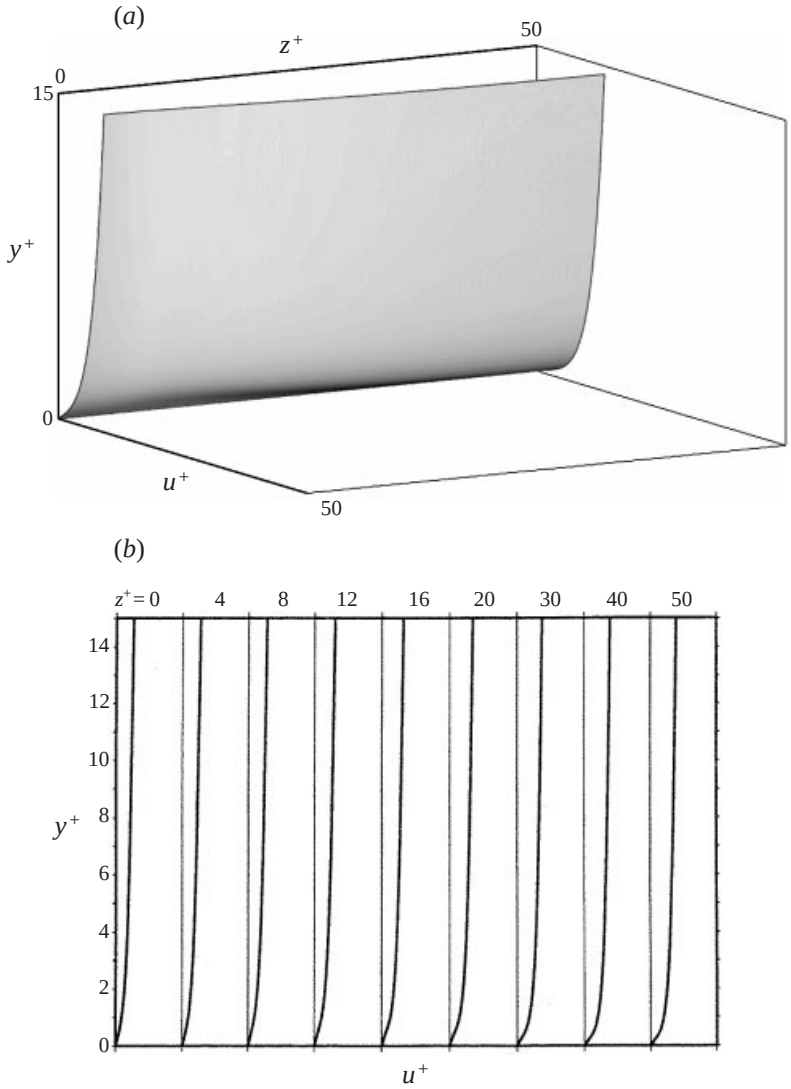

FIGURE 7 (a, b). For caption see page 27.

move outward near the $z^+ = 0$ boundary; as this occurs, the low-speed dimple in the streamwise velocity surface contour shown in figure 7(g) also moves dramatically outward to occupy the region from $y^+ = 0$ to 30 near the $z^+ = 0$ boundary. The flow is independent of the streamwise direction, and if hydrogen bubbles or dye were injected in such a flow field near $y^+ = 0$, a prominent low-streamwise speed region would be marked near $z^+ = 0$, particularly at the dimple; this region would move toward the symmetry plane at $z^+ = 0$ and outward towards y_∞^+ with time. The profiles of $u^+(y^+)$ at $\tau = 9.1$ in figure 7(h) show a highly inflectional behaviour coincident within the recirculation region of the crossflow streamlines depicted in figure 3(e). With increasing Reynolds number, the streamwise behaviour becomes more severe and complex. An example is shown in figure 8 at $Re_\lambda = 50\,000$, where the dimple thins and moves rapidly outward toward the outer boundary with time. The region near the dimple is characterized by multiple inflection points in streamwise velocity,

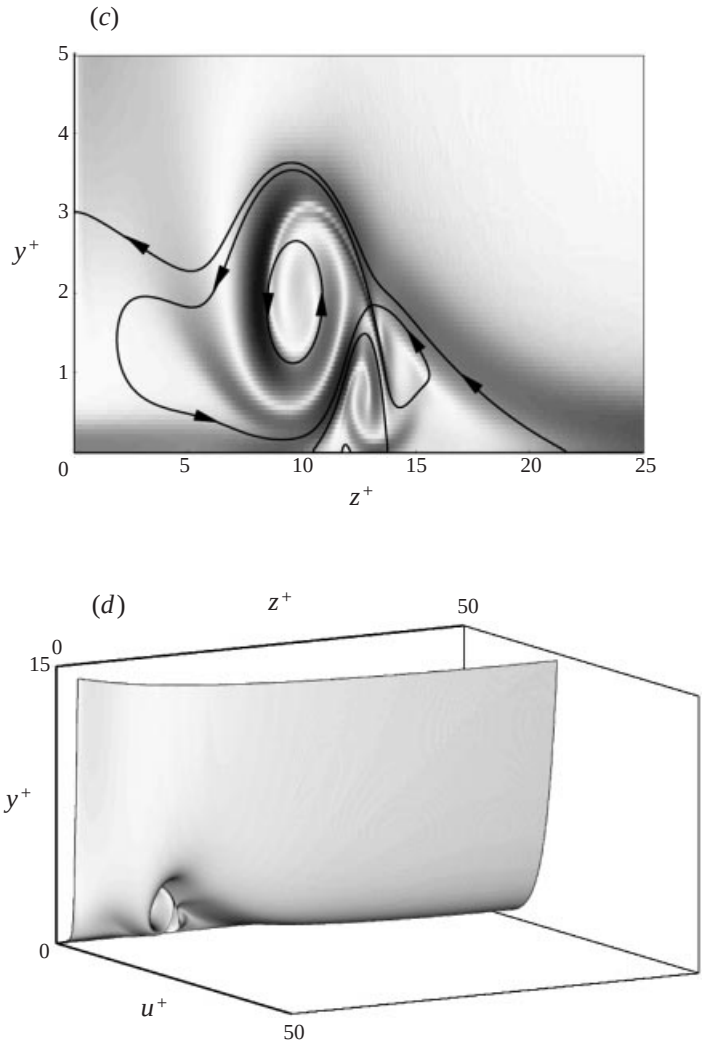

FIGURE 7 (c, d). For caption see page 27.

as well as significant ranges in the normal direction where the velocity is almost zero. This case is believed to be approaching to the limit of what can be computed accurately with the current computational resources.

Before discussing phenomenology related to the present results, it is important to address the question of whether the apparent instability in the crossflow solution is physical or whether it might be associated with the numerical solution. First, the effect of computational mesh size will be discussed. In all cases, initial calculations were carried out with a uniform mesh in the y^+-, z^+-directions, with the finest mesh having 400 and 1000 points, respectively. At higher values of Re_λ, the vorticity contours began to develop a noise-like character typical of that shown in figure 9(a) at $\tau = 2.86$ for $Re_\lambda = 50\,000$. This apparent anomaly was always associated with the spanwise location of the alleyway predicted in the crossflow streamlines. In order to better resolve this region, the mesh transformations (28) were introduced. As increasing numbers of mesh points in z^+ were focused into the zone near where the alleyway

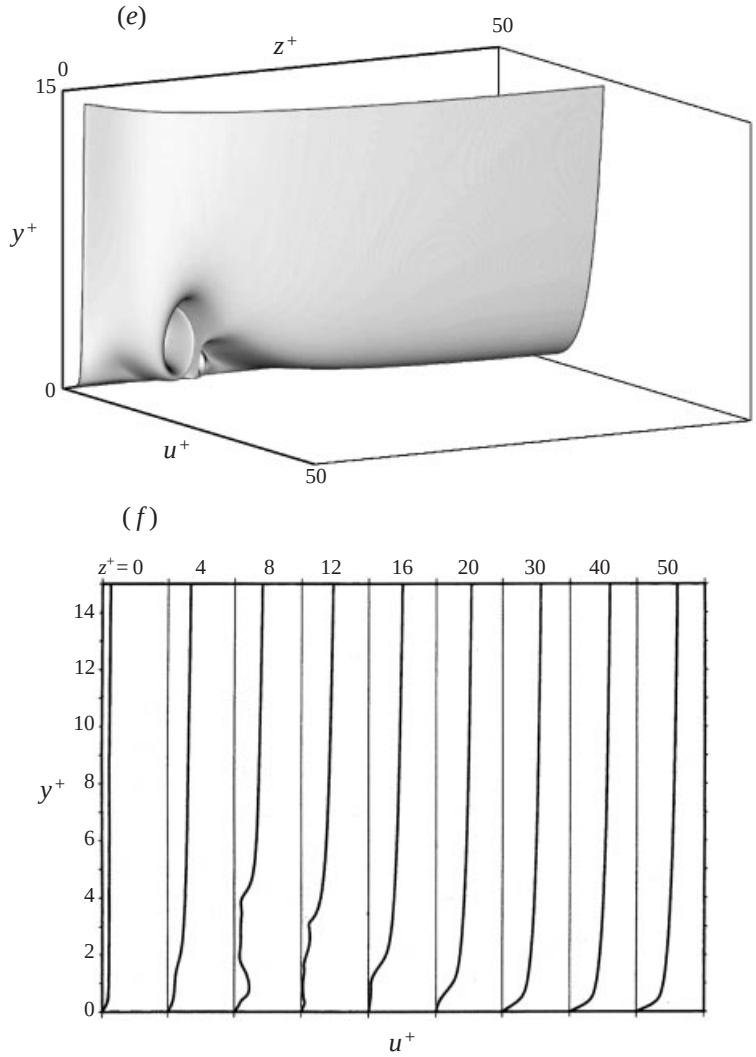

FIGURE 7 (*e*, *f*). For caption see facing page.

ultimately appears, the vorticity contours more clearly revealed the wavelike instability shown in figures 9(*b*) and 9(*c*). The value of $\beta = 6$ in figure 9(*c*) provides a tighter concentration of points around $z^+ = 14.3$ than for $\beta = 5$ in figure 9(*b*). Although the growth of the instability in figure 9(*c*) slightly lags that in figure 9(*b*), the evolving wavelike character is identical. The uniform mesh size for figure 9(*a*) is $\Delta z^+ = 0.05$, while $\Delta z^+ = 0.019$ and 0.014 at $z^+ = 14.3$ for $\beta = 5$ and 6, respectively. A subsequent lengthy calculation with 400 and 1500 points in the normal and spanwise directions showed the same evolution as in figure 9(*c*). Note that for values of β significantly larger than 6, the mesh in the z^+-direction is heavily skewed across the span, and poor convergence of the solution was experienced. The use of the spanwise mesh transformation provided the necessary spatial resolution in the vicinity of the initial instability and made it possible to carry the calculation forward in time. As shown in figure 4, vorticity oscillations subsequently appear at secondary sites associated with new alleyway formation. Transformations which focus points into multiple regions are,

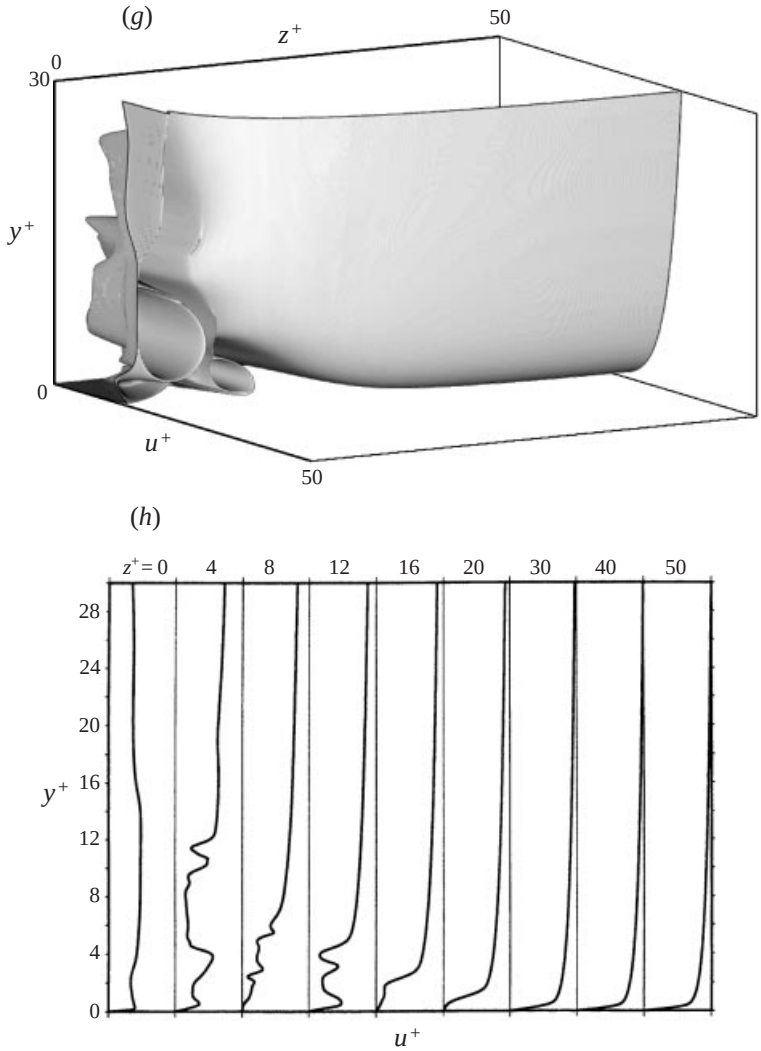

FIGURE 7. (a, b) Streamwise velocity for $Re_\lambda = 10\,000$. (a) $\tau = 1.0$; surface contour of velocity magnitude; (b) $\tau = 1.0$; profiles at selected z^+ stations. (c, d) Streamwise velocity for $Re_\lambda = 10\,000$. (c) $\tau = 3.35$; front view of surface contour of low-speed dimple with crossflow streamlines overlaid; (d) $\tau = 3.35$; isometric view of velocity magnitude. (e, f) Streamwise velocity for $Re_\lambda = 10\,000$. (e) $\tau = 3.95$; surface contour of velocity magnitude; (f) $\tau = 3.95$; profiles at selected z^+ stations. (g, h) Streamwise velocity for $Re_\lambda = 10\,000$. (g) $\tau = 9.1$; surface contour of velocity magnitude; (h) $\tau = 9.1$; profiles at selected z^+ stations.

in principle, possible but were not attempted here because of the complex unsteady behaviour of the solution. Although the spanwise transformation (28) focuses the computational mesh about one point Z_o, the resolution in the neighbourhood of Z_o, including the locations of later instabilities, is finer than that of the uniform mesh and apparently adequate to resolve the wavelike character. Moreover, the subsequent occurrences of the instability appear to be essentially similar to the first, which was clearly well resolved.

A number of other aspects of the calculations were also checked. First, consider the timestep. Many sensitivity calculations were carried out, especially at the higher

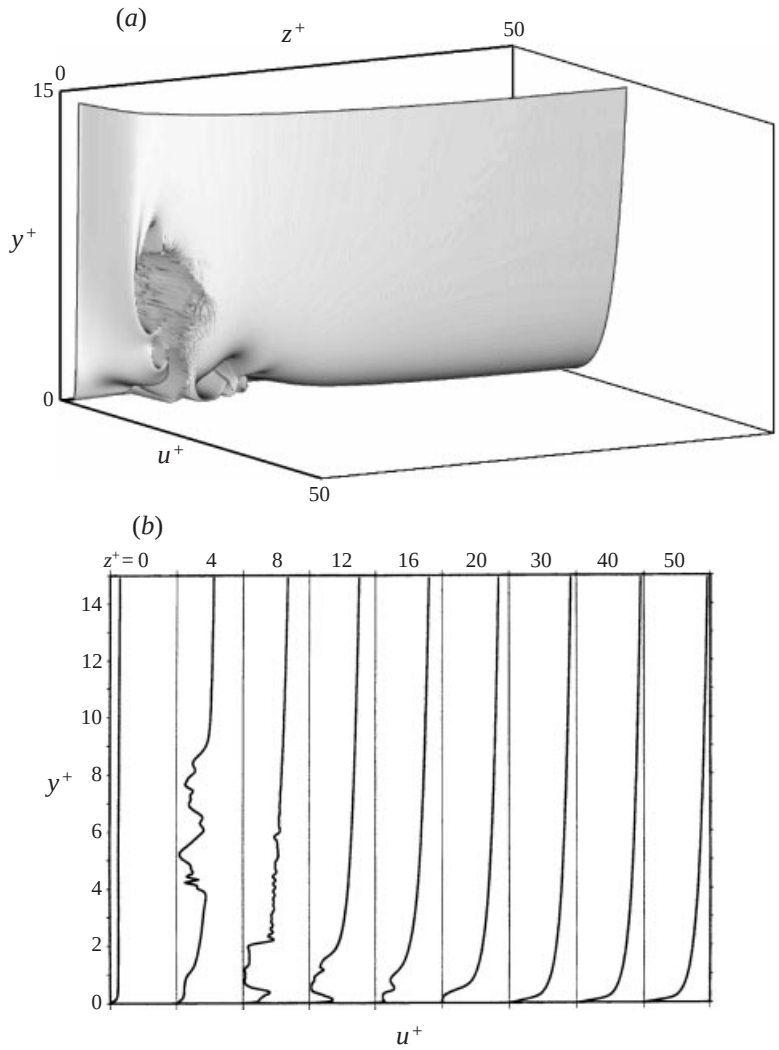

FIGURE 8. (a, b) Streamwise velocity for $Re_\lambda = 50\,000$. (a) $\tau = 4.34$; surface contour of velocity magnitude; (b) $\tau = 4.34$; profiles at selected z^+ stations.

Reynolds numbers, where more intense activity occurred at smaller timescale, and it was determined that a step of $\Delta\tau = 0.001$ was adequate for all Reynolds numbers considered. In particular, for $Re_\lambda = 50\,000$, calculations were also run for $\Delta\tau = 0.0005$ and 0.0001, and the results showed that the development of the wavelike instability was independent of timestep. This suggests that the instability is not a consequence of insufficient temporal resolution. Secondly, to check that the predicted oscillations were not related to inadequate iteration convergence, the case for $Re_\lambda = 50\,000$ was rerun in its entirety with the relative convergence criterion on the vorticity, stream function and streamwise velocity solutions reduced from 10^{-4} to 10^{-5}; again, no significant differences in the solutions were observed. Thirdly, a referee has suggested that use of the SOR algorithm for the stream function equation may be suspect, and

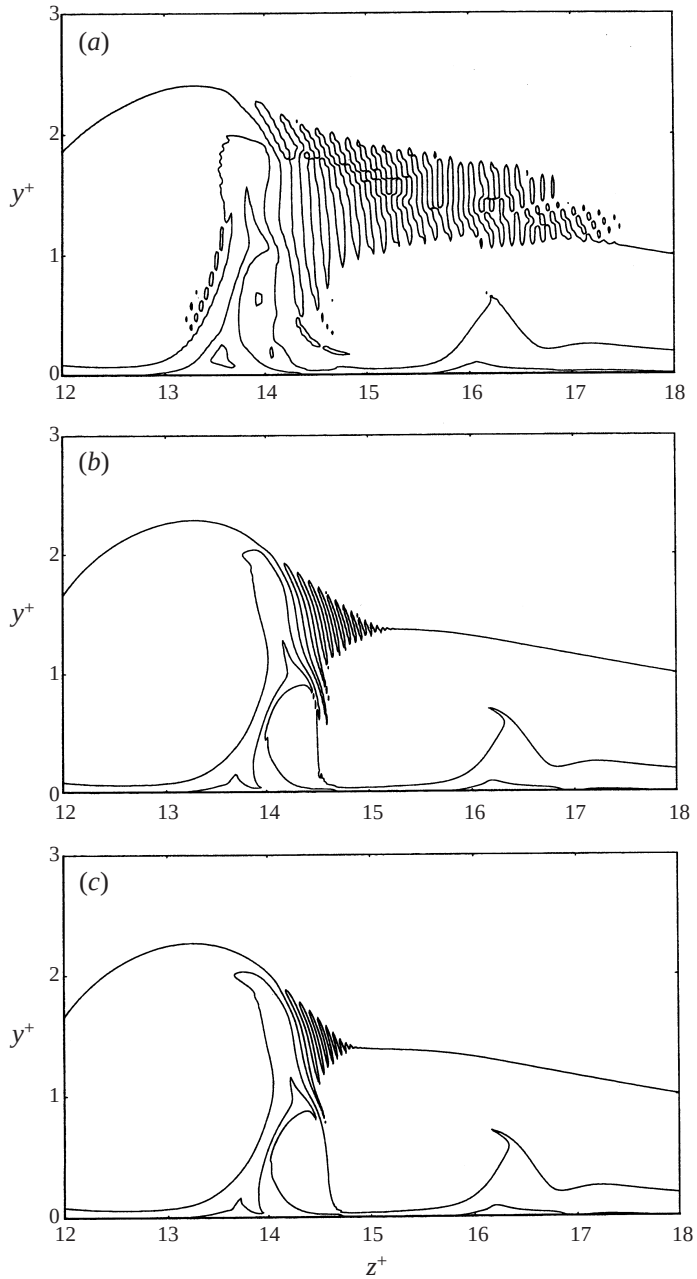

FIGURE 9. (*a–c*) Mesh sensitivity results for $Re_\lambda = 50\,000$ at $\tau = 2.86$. Zero-vorticity contours. (*a*) spanwise uniform mesh; (*b*) spanwise transform with $\beta = 5$; (*c*) spanwise transform with $\beta = 6$.

so the calculations were also rerun using standard Gauss–Seidel iteration; again, no differences were observed.

Lastly, to provide further confidence that the phenomena predicted in the finite-difference solutions are physical, spectral calculations were performed at several Reynolds numbers for comparison. As discussed in § 4, the number of Fourier modes required to resolve the crossflow solution beyond a certain stage quickly became

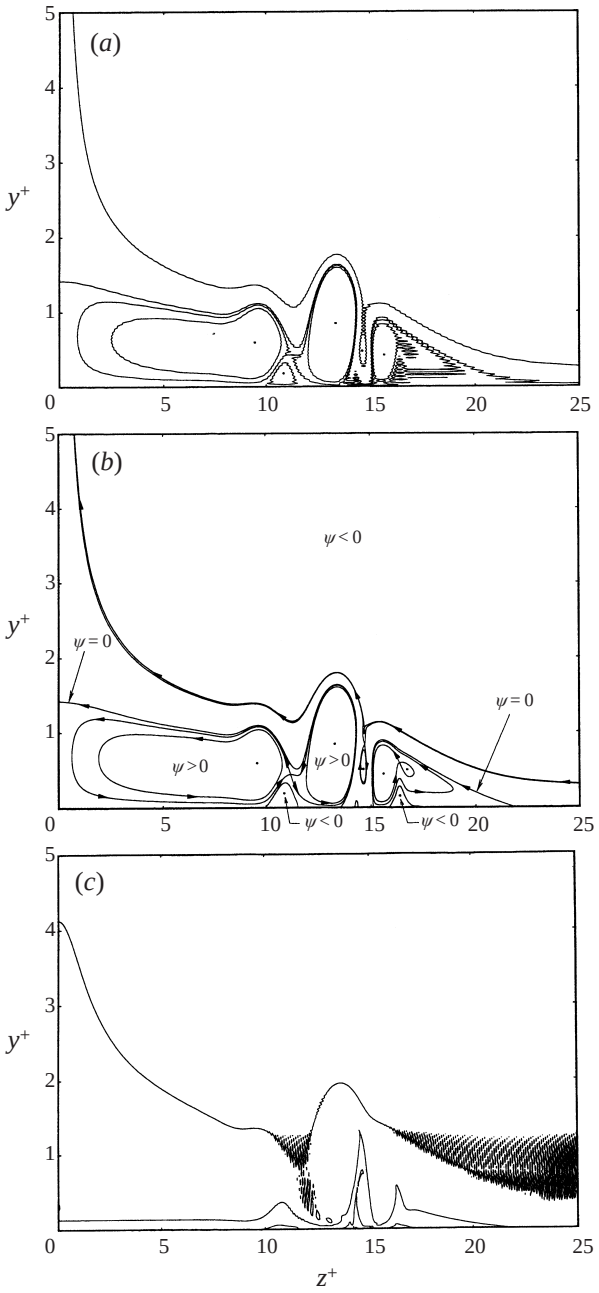

FIGURE 10 (*a–c*). For caption see facing page.

prohibitively large at high Re_λ. The spectral solutions did, however, verify the prediction of some prominent features, including the alleyway in the crossflow streamlines, vorticity fingers protruding from the wall, wall-shear spikes, and the low-speed dimple in the streamwise velocity. Detailed comparisons between the two methods are given by Brinckman (1996), and here the spectral results will be summarized briefly. At early times for any Re_λ, the two methods give virtually identical results. However, as

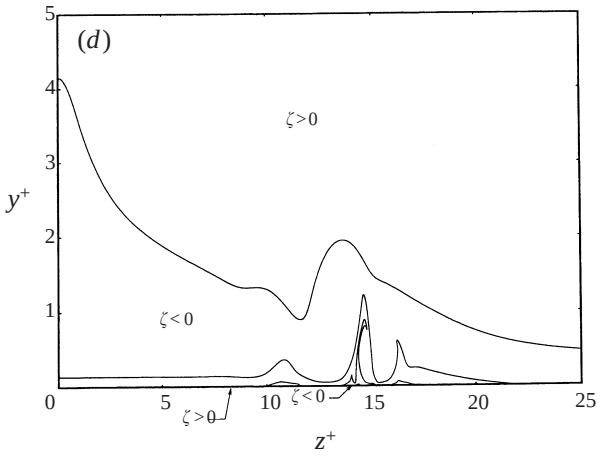

FIGURE 10. (*a*, *b*) Comparison of finite-difference and spectral solution for $Re_\lambda = 50\,000$ at $\tau = 2.76$; (*a*) crossflow streamlines form spectral solution; (*b*) crossflow streamlines from finite-difference solution. (*c*) Streamwise vorticity from spectral solution; (*d*) streamwise vorticity from finite-difference solution.

the crossflow solution becomes increasingly complex, eventually the spectral method is unable to cope with the developing intense variations in the spanwise direction, even with more than 800 terms. Significant anomalies with the spectral method first show up in the vorticity field where high-frequency oscillations are seen over an area in the computational domain; this behaviour is eventually observed in the streamlines. As an example, consider the results shown in figure 10 for $Re_\lambda = 50\,000$ at $\tau = 2.76$, where oscillations over a substantial portion of the field occur in the spectral method; at a previous time $\tau = 2.57$, the streamline patterns by either method are identical (Brinckman 1996), but oscillations occur in the spectral solution for the vorticity field over a substantial part of the computational domain. It is worthy of note that both methods predict the formation of a primary alleyway (figure 10*a*, *b*), as well as the corresponding vorticity finger (figure 10*c*, *d*). At this point in the spectral calculation, 666 Fourier modes were required to produce the resolution shown and, although the onset of oscillations in the spectral method can be briefly delayed by introducing additional Fourier modes, it is evident that the spectral method is not useful by this stage. Furthermore, the spectral technique could not be counted on to reliably detect the instability that occurs soon after $\tau = 2.76$. This difficulty with spectral methods is reasonably well known. If the flow field is relatively smooth in space, a spectral technique is accurate and typically more efficient than a corresponding finite-difference method. However, if local regions of intense variation start to form, an increasing number of terms are required in a spectral method, and, ultimately, a failure can occur (of the type depicted in figure 10), where the entire solution is corrupted by spurious high-frequency oscillations. In contrast, in a finite-difference method, computational resources can be focused in regions of intense variation through use of a non-uniform mesh. The calculations can then be continued reliably beyond the stage shown in figure 10 when the instability develops.

6. Discussion

A number of aspects emerge from the present study which are consistent over the range of Reynolds numbers investigated and which are probably relevant in other

two-dimensional problems involving separation. In addition, the results may offer some insight into the dynamics of a turbulent boundary-layer flow, as well as a further possible mechanism for regeneration other than that described by Smith *et al.* (1991). The principal features of the wall-layer evolution observed here are: (i) the development of a concentrated region of severely retarded streamwise velocity near the common outflow plane between vortices, which is accompanied by inflectional behaviour in the streamwise velocity profiles; (ii) the formation of a recirculation zone in the crossflow plane and the continual splitting of this region to produce numerous eddies at progressively smaller scales; (iii) the formation of alleyways in the crossflow recirculation region, which precede the vorticity oscillations and provide the physical mechanism which eventually drives the instability; (iv) the onset of high-frequency oscillations in the streamwise vorticity contours at sufficiently high values of Reynolds number, suggesting the onset of a wall-layer instability; and (v) a strong correlation between the occurrence of a sharp peak in local wall shear and the subsequent onset of the vorticity oscillations. In this section, these features are discussed, as well as the possible relationships to the turbulent boundary layer.

Consider first the streamwise problem. Fluid with high streamwise momentum in the outer part of the boundary layer is carried in towards the wall by the vortex motion at periodic spanwise intervals (e.g. $z^+ = 50$), and near the down-flow side of the vortex, the streamwise profiles are relatively full. A local deceleration of the streamwise velocity must take place to satisfy the no-slip condition at the wall. The action of the external vortex sweeps this fluid with low streamwise momentum toward the outflow side of the vortex, and lifts it away from the wall. Thus, the streamwise profiles near the outflow plane (e.g. $z^+ = 0$) are much less full, where low-speed fluid then displaces high-speed fluid above. The foregoing discussion is the common kinematical explanation of why alternate regions of high- and low-speed flow are observed in the turbulent wall layer, but is less revealing of other behaviour associated with the low-speed streaks. The present results suggest additional dynamical features that may be useful in the interpretation of near-wall turbulent behaviour. Once crossflow recirculating eddies occur, the streamwise velocity profiles on the outflow side of the vortex develop inflection points, and in the surface contours of streamwise velocity, a dimple of severely retarded streamwise velocity forms near the $z^+ = 0$ boundary; this would appear as part of a low-speed streak. The significance of the dimple is that low-speed fluid becomes trapped near the wall by the recirculating eddies in the crossflow, as illustrated in figures 7(*c*) and 7(*d*), rather than merely being decelerated at the wall and then swept outward. This concept of a concentrated dimple of low-speed fluid appears consistent with the observations of Kline *et al.* (1967), who remarked that low-speed streaks persist right to the wall and drift slowly outward with time, thinning as they move out of the inner region and beginning to oscillate when they reach $y^+ \sim 8$–12 (see figure 7). An interesting feature of the unstable range of Reynolds numbers ($Re_\lambda \geqslant 35\,000$) in the present study is that the dimple grows outward in close proximity to the region of instability in the crossflow plane, suggesting that in a fully three-dimensional simulation the crossflow instability may impart an oscillatory type of effect to the low-speed region, consistent with the oscillations of low-speed streaks observed by Kline *et al.* (1967), Kim *et al.* (1971), Acarlar & Smith (1987*b*), and Swearingen & Blackwelder (1987).

Inflectional behaviour is a common criterion used for assessing the potential instability of a predominantly streamwise flow since a necessary condition for an inviscid instability in steady flow is that the base profile $u(y)$ must have a point of inflection at y_0. In their experimental investigation of the breakdown of Görtler

vortices, Swearingen & Blackwelder (1987) found that both the spanwise and streamwise velocity profiles became inflectional. A close correlation between spanwise shear ($\partial u/\partial z$) and oscillations in streamwise velocity in their measurements led Swearingen & Blackwelder (1987) to conclude that peaks in the spanwise shear were the main precursor of instability. In an experimental study of the role of streamwise vortices in the transition to turbulence, Hamilton & Abernathy (1994) also identified inflectional profiles in both spanwise and streamwise velocity profiles for both laminar and transitional flow over a flat plate. The observation that laminar flows exhibited inflectional behaviour led Hamilton & Abernathy (1994) to the conclusion that a simple argument based on the presence of an instantaneous inflection point is inadequate for predicting instability. A similar observation was reported for turbulent boundary-layer flow by Kim *et al.* (1971) who suggested that although the occurrence of an instantaneous inflectional streamwise velocity profile often leads to a growing oscillation and breakup, it does not always do so. Thus, the significance of inflectional velocity profiles in a time-dependent (and often non-parallel) flow as a predictor of boundary-layer instability and bursting remains uncertain. In the present study, severe distortions of the streamwise and spanwise profiles were produced by the convective effects associated with the crossflow recirculating eddies. The results for $Re_\lambda = 10\,000$ in figure 7(f) clearly show inflection points in the $u^+(y^+)$ profiles at $z^+ < 30$. The inflectional behaviour worsens with an increase in time as the low-speed dimples become more prominent in the surface contours of streamwise velocity magnitude (figure 7(h)). However, as time proceeds, the inflectional behaviour does not lead to a breakdown of the $Re_\lambda = 10\,000$ solution. Note, however, that the present simulation is limited because the motion is independent of the streamwise coordinate; in a full three-dimensional model, it is possible that instability associated with the streamwise profiles could occur. Inspection of spanwise and streamwise profiles for the unstable case of $Re_\lambda = 50\,000$ at times $\tau = 2.76$ and $\tau = 2.96$ shows that inflectional points exist both before and after the onset of the crossflow instability at $\tau = 2.83$ (Brinckman 1996). The crossflow solution is independent of the streamwise solution, and despite the highly inflectional profiles in streamwise velocity, the mechanism driving the crossflow instability is associated only with the crossflow solution.

The prediction of a crossflow instability at finite Reynolds number is significant. For the case of infinite Reynolds number, Van Dommelen & Shen (1980) showed that an unsteady separation singularity occurs at finite time ($\tau \approx 3$) for an impulsively started cylinder. The limit problem $Re_\lambda \to \infty$ here is identical to that for the circular cylinder and thus develops a singularity in the crossflow solution (Walker & Herzog 1988). In contrast, the present Navier–Stokes solutions predict an instability in the crossflow plane which exhibits high-frequency oscillations in the streamwise vorticity around $\tau = 3$ that grow steadily with time. These solutions do not develop a focused eruptive behaviour, even by the stage where the calculations were terminated. This suggests that either the spanwise diffusion term in the crossflow momentum equations or normal pressure gradients (see, for example, Li *et al.* 1998) act to suppress the sharp eruptive behaviour predicted at infinite Reynolds number; in any event, the crossflow eddies bifurcate and oscillations develop in the streamwise vorticity without a focused breakdown. In the transitional range, the vorticity oscillations are evidently suppressed by viscous effects as the recirculating eddies confine the instability to the near-wall region. In the unstable range, the oscillations propagate all the way to the outer flow and this behaviour ultimately terminates the calculation. Considerable effort was made to extend the calculations to higher Re_λ and, in particular, to $Re_\lambda = 10^5$, in an effort to tie on to the characteristics of the limit solution $Re_\lambda \to \infty$ (Walker &

Herzog 1988). The protruding growth of the primary eddy shown in figure 2(*e*) for $Re_\lambda = 50\,000$ becomes progressively narrower as Re_λ was increased to 75 000 and then to 10^5; for $Re_\lambda = 10^5$, it occupies a spanwise range of $\Delta z^+ \simeq 1$, thereby indicating a possible tendency toward a spiky response as $Re_\lambda \to \infty$. However, for $Re_\lambda = 10^5$, multiple narrow alleyways opened up in the range $z^+ = 10$–18, and oscillations were observed around $\tau \approx 2.4$ as the vorticity instability penetrated the external flow. Unfortunately, at this Reynolds number, there is so much intense activity occurring at multiple sites that some of the calculated solution details were not considered reliable, despite the fact that maximum computational resources were used.

A prominent feature of the solutions at finite Re_λ produced in this study, which is absent in the limit problem ($Re_\lambda \to \infty$), is the formation of alleyways in the crossflow recirculating eddies. The alleyways appear to be a plausible generic phenomena in flows separating at high Reynolds numbers and provides a mechanism wherein sharp gradients in wall shear are generated and wall effects are convected outward. High-frequency bursts have not been seen in transition in free-shear layers (Maslowe 1985) suggesting that viscous wall effects must play an important role in the wall-layer breakdown. The present results point to the potential importance of alleyways in the crossflow recirculation zones as a mechanism for communication between the outer flow and the wall, in addition to the focused eruptions known to occur for very high Re_λ (Van Dommelen & Shen 1980; Smith *et al.* 1991; Smith & Walker 1995). Here, the central characteristics of the instability process and the relation to alleyway formation are summarized:

(*a*) In the transitional and unstable range of Reynolds number discussed in § 5, the alleyways convect wall-generated vorticity outward in finger-like protuberances resulting in a focused interaction of positive wall-generated vorticity with the positive vorticity of the outer flow. The interaction occurs shortly after oscillations appear in the streamwise vorticity just upstream. For stable cases (e.g. $Re_\lambda = 10\,000$), the initial alleyway subsides before an interaction with the outer flow occurs; a crossflow instability does not occur.

(*b*) The high-frequency oscillations in the streamwise vorticity occur only at locations where alleyways form.

(*c*) An alleyway always produces a negative spike in spanwise wall shear, $(\partial w^+/\partial y^+)$ at $y^+ = 0$, analogous to the peaks in vorticity observed by Loc & Bouard (1985) on the wall of a circular cylinder. This spike in wall shear peaks immediately prior to the onset of oscillations in the streamwise vorticity, and is a consistent precursor of the crossflow instability. This result holds for instabilities in the primary alleyway as well as in all subsequent alleyways.

(*d*) The magnitude of the negative wall shear peak that occurs just prior to the onset of instability increases with Reynolds number (Brinckman 1996). For a given Reynolds number, the largest magnitude of the wall-shear peak generally occurs for the first alleyway.

(*e*) As Reynolds number is increased, the time to formation of the alleyway and onset of the initial instability decreases in a consistent manner, as shown in table 2. There is some uncertainty concerning the quality of the solutions for the two highest Reynolds numbers, however, and it was not possible to determine whether $\tau_{instability}$ approaches a finite limit as $Re_\lambda \to \infty$. It may be noted that the limit problem $Re_\lambda \to \infty$ reaches a singularity at $\tau = 3$.

For the results quoted in table 2, for sufficiently high Re_λ, the onset of instability precedes the time of evolution of a spike in the limit problem ($Re_\lambda \to \infty$). This is to some extent consistent with the limit analysis of Cassel *et al.* (1996), who show that a

Re_λ	$\tau_{instability}$
20 000	3.75
30 000	3.15
35 000	3.04
50 000	2.83
75 000	2.6
100 000	2.4

TABLE 2. Time to the onset of instability versus Reynolds number.

high-frequency instability develops along the zero vorticity line, prior to the formation of a separation singularity, in the first interactive stage of separation as $Re_\lambda \to \infty$. However, it is far from clear that the two instabilities are related, since the work of Cassel *et al.* (1996) depends crucially on the occurrence of a singularity; the present results suggest that an instability comes into play well before there is any evidence of the onset of a singularity. The high Re_λ problem is apparently characterized by multiple types of instability and even the limit problem $Re_\lambda \to \infty$ may contain a large wavenumber instability (Cowley, Hocking & Tutty 1985). It is also worthwhile to note that interacting boundary-layer theory does predict the bifurcation of a primary recirculation zone into multiple eddies in vortex-induced separation (Peridier *et al.* 1991*b*), as observed in the present study. However, the formation of the alleyways and the subsequent instability is only revealed through the present Navier–Stokes calculations. The present results are also similar to those obtained recently by Li *et al.* (1998) who have considered the next stages of interaction beyond that described by conventional interacting boundary-layer theory. These authors consider a further stage where normal pressure gradients come into play, and this stage is then followed by a process of strong wind-up into a local vortex, again suggestive of the formation of multiple vortices. It may be noted that calculated results for the perturbation pressure p_1 (Brinckman 1996) show intense variations in the pressure near the wall in both the spanwise and normal directions, particularly near the alleyways.

A referee has suggested that the present instability is likely to be a Rayleigh instability which can occur once there is an inflection point in the crossflow profile w^+. It is true that there are multiple inflection points in w^+ within the alleyways. If the present instability is related to a Rayleigh instability, the wavenumber should scale like $Re_\lambda^{1/2}$. The wavenumber k was determined from the numerical solutions as follows. Once the onset of the vorticity instability was detected and at least eight cycles were observed, the wavenumber was estimated from the graphs of the zero vorticity line in the z^+ coordinate using the four most recently formed cycles (see, for example, the waves between $z^+ \simeq 14.1$ and 14.3 in figure 4(*c*)). As the wave forms, it is stretched out to the left end by convective effects, and so the uniform criterion discussed for each Re_λ was adopted. This is clearly an *ad hoc* criterion and the determination of k from a wave in a complex flow field is necessarily imprecise and somewhat objective. In any event, the values of k obtained in this manner do show a trend and the raw data are shown in figure 11 (note that the wavenumbers identified by this process for each Re_λ were identical for values of $Y_{\max}$ other than those quoted in table 1). A least-squares regression analysis for the function $k = C_o Re^{\beta_o}$ produced values of $C_o = 0.546$ and $\beta_o = 0.5$. Although some scatter is expected in the values of k about this curve, it may be seen that the data in figure 11 are reasonably well

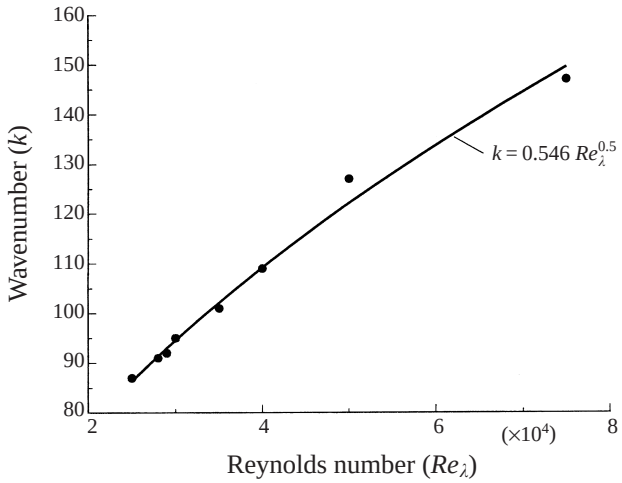

FIGURE 11. Estimated wavenumber k for the onset of the instability and least-squares curve fit.

represented. This would seem to support the notion that the present instability is a Rayleigh instability.

Several features predicted in the present study appear consistent with experimental investigations of turbulent boundary-layer flow. Peaks in wall shear and wall pressure have been reported as a precursor to the burst-sweep cycle in a turbulent boundary layer by Thomas & Bull (1983) in wind-tunnel tests. Thomas & Bull (1983) discuss peaks in measured wall pressure and a local deceleration of the velocity parallel to the wall which they associated with large-scale motions due to the convection of horseshoe vortices above the wall layer. Although the orientation of the outer-layer flow structure considered in the present study may differ from that investigated by the previous authors, several features related to the formation of the present alleyway seem consistent with their findings. Calculated results for the pressure perturbation p_1 (Brinckman 1996) show a strong local variation in wall pressure associated with the alleyways. This behaviour is consistent with the observations of Thomas & Bull (1983), where strong wall-pressure variations are associated with a shear layer which penetrates close to the wall just prior to a burst event. Furthermore, streamwise velocity profiles, located in the alleyway region between $z^+ = 13.5$ and $z^+ = 15.5$ in figure 10(*b*) (Brinckman 1996), illustrate how a portion of the alleyway draws fluid of relatively higher streamwise velocity in towards the wall between $z^+ = 15.0$ and $z^+ = 15.1$ in a region of otherwise strongly decelerated flow; this is reminiscent of the 'pockets' described by Falco (1991), which are free of marker in an otherwise marked turbulent wall layer. These comparisons to previous findings are not intended to suggest that the precise structure of a turbulent boundary layer has been captured with the present model. They do, however, demonstrate that there are features of the present model problem and associated alleyway formation which are common to observed characteristics of turbulent boundary-layer flow.

Finally, the question of how the predicted vorticity oscillations would be manifest in visualizations of the flow is of interest. In a steady flow, streamlines represent particle paths, and bubbles or other markers injected into the flow follow the streamlines. In an unsteady flow, however, the instantaneous streamlines are not entirely revealing about prior events and the instability is not apparent in the streamline plots. The

vorticity oscillations here are far from the wall and are centred on the zero vorticity contour. As oscillations develop on the zero-vorticity line in an essentially inviscid region, particles making up the material line will also experience the oscillations; this suggests that markers in the flow would reveal the predicted instabilities.

7. Conclusions

An instability in the developing wall layer beneath a counter-rotating vortex pair has been identified in solutions of the Navier–Stokes equations at high Reynolds numbers. The instability appears in the form of relatively high-frequency wavelike oscillations in the streamwise vorticity contours which grow in amplitude with time. Considerable effort has been expended to ensure that the observed oscillations are grid independent. At sufficiently high Reynolds numbers, the oscillations eventually penetrate the outer-flow region, suggesting that a breakdown of the local flow structure is imminent. Detailed calculations show that alleyways between the outer-flow region and the wall open up in the crossflow recirculating regions within the wall layer, as it undergoes a process of continuous subdivision to finer scales. The formation of the alleyway provides the mechanism for a strong local interaction with the outer flow which appears to provoke the predicted instability. While the eddying crossflow motion drives inflectional behaviour of the streamwise velocity profiles, there is no evidence of unstable behaviour of the streamwise flow. As the Reynolds number is increased, the near-wall activity in the crossflow solution becomes more intense, but the instability continues to develop without a focused eruption of the crossflow streamlines. Thus, the present instability provides another potential route to breakdown of a viscous wall-layer flow, in addition to the focused eruption process identified by Van Dommelen & Shen (1980, 1982) for the case corresponding to $Re_\lambda \to \infty$.

The present study may be important in a wider context (S. J. Cowley, private communication), and the following paraphrases his comments (see also Cowley & Stewart 2000). It has long been hoped that as the Reynolds number, Re, increases, the unsteady boundary-layer equations would provide an asymptotic solution, as $Re \to \infty$, to the Navier–Stokes equations which can be realized. It has been known for some time that solutions to the unsteady boundary-layer equations are unstable to very rapidly growing short wavelength disturbances (see, for example, Tutty & Cowley 1986); however, it has been thought that if such disturbances were not introduced artificially by significant rounding or truncation errors, then these instabilities would not invalidate unsteady boundary-layer solutions that were carefully computed. The reasoning behind this viewpoint was that although the growth rate of the instabilities is large, the amplitude of high-wavenumber modes generated by nonlinear self-interactions would be so small that their growth by Rayleigh instabilities, etc. would not be sufficient to prevent a boundary-layer calculation being carried out smoothly up to, say, the point where the solution terminates in a Van Dommelen singularity. This study provides evidence that the above view may not be correct and that terms which are initially small can grow to disrupt the solution. On the basis of our calculations, Cowley & Stewart (2000) have suggested a scaling argument that supports this evidence for a boundary-layer flow, and demonstrates that the same scaling argument applied to the certain asymptotic regimes of the Kuramoto–Sivashinsky equation predicts similar behaviour that can be numerically confirmed.

The authors would like to thank the referees for a number of helpful comments.

This work was supported in part by the United States Army Research Office under grant no. 40019-DAAD19-99-1-0244.

REFERENCES

Acarlar, M. S. & Smith, C. R. 1987*a* A study of hairpin vortices in a laminar boundary layer. Part 1. Hairpin vortices generated by a hemisphere protuberance. *J. Fluid Mech.* **175**, 1–41.

Acarlar, M. S. & Smith, C. R. 1987*b* A study of hairpin vortices in a laminar boundary layer. Part 2. Hairpin vortices generated by fluid injection. *J. Fluid Mech.* **175**, 43–83.

Asai, M. & Nishioka, M. 1995 Boundary-layer transition triggered by hairpin eddies at subcritical Reynolds numbers. *J. Fluid Mech.* **297**, 101–122.

Bakewell, H. P. & Lumley, J. L. 1967 Viscous sublayer and adjacent wall region in turbulent pipe flow. *Phys. Fluids* **10**, 1880–1889.

Blackwelder, R. F. 1983 Analogies between transitional and turbulent boundary layers. *Phys. Fluids* **26**, 2807–2815.

Bouard, R. & Coutanceau, M. 1980 The early stage of development of the wake behind an impulsively started cylinder for $40 < Re < 10^4$. *J. Fluid Mech.* **101**, 583–607.

Brinckman, K. W. 1996 An instability in vortex/wall-layer interactions at high Reynolds number. PhD thesis, Department of Mechanical Engineering and Mechanics, Lehigh University, Bethlehem, PA.

Cassel, K. W., Smith, F. T. & Walker, J. D. A. 1996 The onset of instability in unsteady boundary-layer separation. *J. Fluid Mech.* **315**, 223–256.

Chapman, D. R. & Kuhn, G. D. 1986 The limiting behaviour of turbulence near a wall. *J. Fluid Mech.* **170**, 265–292.

Chernyshenko, S. I. 1988 The asymptotic form of the stationary separated circumference of a body at high Reynolds number. *Prikl. Matem. Mekh.* **52**, 958–966.

Chernyshenko, S. I. 1998 Asymptotic theory of global separation. *Appl. Mech. Rev.* **51**, 523–536.

Cowley, S. J. & Stewart, P. A. 2000 Laminar boundary-layer theory: a 20th century paradox? *Proc. 20th Intl Congr. of Theoret. and Appl. Mech.* Chicago, IL.

Cowley, S. J., Hocking, L. M. & Tutty, O. R. 1985 The stability of solutions of the classical unsteady boundary-layer equation. *Phys. Fluids* **28**, 441–443.

Cowley, S. J., Van Dommelen, L. L. & Lam, S. T. 1990 On the use of Lagrangian variables in descriptions of unsteady boundary-layer separation. *Phil. Trans. R. Soc. Lond.* A **333**, 343–378.

Degani, A. T., Walker, J. D. A. & Smith, F. T. 1998 Unsteady separation past moving surfaces. *J. Fluid Mech.* **375**, 1–38.

Doligalski, T. L., Smith, C. R. & Walker, J. D. A. 1994 Vortex interactions with walls. *Ann. Rev. Fluid Mech.* **26**, 573–616.

Ece, M. C., Walker, J. D. A. & Doligalski, T. L. 1984 The boundary layer on an impulsively started rotating and translating cylinder. *Phys. Fluids.* **27**, 1077–1089.

Elliott, J. W., Cowley, S. J. & Smith, F. T. 1983 Breakdown of boundary layers: (i) on moving surfaces; (ii) in self-similar unsteady flow; (iii) in fully unsteady flow. *Geophys. Astrophys. Fluid Dyn.* **25**, 77–138.

Ersoy, S. & Walker, J. D. A. 1986 Flow induced at a wall by a vortex pair. *AIAA J.* **24**, 4597–1605.

Falco, R. E. 1991 A coherent structure model and its ability to predict Reynolds number dependence. *Proc. Roy. Soc. Lond.* A **336**, 103–129.

Fornberg, B. 1985 Steady viscous flow past a circular cylinder up to Reynolds number 600. *J. Comput. Phys.* **61**, 297–320.

Haidari, A. H. & Smith, C. R. 1994 The generation and regeneration of single hairpin vortices. *J. Fluid Mech.* **277**, 135–162.

Hall, P. & Horseman, N. J. 1991 The linear inviscid secondary instability of longitudinal vortex structures in boundary layers. *J. Fluid Mech.* **232**, 357–375.

Hamilton, J. M. & Abernathy, F. H. 1994 Streamwise vortices and transition to turbulence. *J. Fluid Mech.* **264**, 185–212.

Hatziavramidis, D. T. & Hanratty, T. J. 1979 The representation of the viscous wall region by a regular eddy pattern. *J. Fluid Mech.* **95**, 655–679.

Head, M. R. & Bandyopadhyay, P. 1981 New aspects of turbulent boundary-layer structure. *J. Fluid Mech.* **107**, 297–338.

Herzog, S. & Walker, J. D. A. 1988 Eruption mechanisms for turbulent flow near walls. In *Transport Phenomena in Turbulent Flows* (ed. M. Hirata & N. Kasagi), pp. 145–156. Hemisphere.

Hinze, S. O. 1975 *Turbulence*. McGraw-Hill.

Hockney, R. W. 1970 The potential calculation and some applications. In *Methods in Computational Physics* (ed. B. Alder, S. Fernbach & M. Rotenberg), pp. 135–211. Academic.

Huang, H. 1991 Incompressible viscous flow in tubes with occlusions. PhD thesis, Department of Mathematics, University of British Columbia.

Huang, H., Modi, V. J. & Seymour, B. R. 1995 Fluid mechanics of stenosed arteries. *Intl J. Engng Sci.* **33**, 815–828.

Huang, H. & Seymour, B. R. 1995 A finite difference method for flow in a restricted channel. *Comput. Fluids* **24**, 153–160.

Kim, H. T., Kline, S. J. & Reynolds, W. C. 1971 The production of turbulence near a smooth wall in a turbulent boundary layer. *J. Fluid Mech.* **50**, 133–160.

Kline, S. J., Reynolds, W. C., Schraub, F. A. & Runstadler, P. W. 1967 The structure of turbulent boundary layers. *J. Fluid Mech.* **30**, 741–773.

Li, L., Walker, J. D. A., Bowles, R. I. & Smith, F. T. 1998 Short-scale break-up in unsteady interactive layers: local development of normal pressure gradients and vortex wind-up. *J. Fluid. Mech.* **374**, 335–378.

Loc, T. P. & Bouard, R. 1985 Numerical solution of the early stage of the unsteady viscous flow around a circular cylinder: a comparison with experimental visualization and measurements. *J. Fluid Mech.* **160**, 93–117.

Maslowe, S. A. 1985 Shear flow instabilities and transition. *Hydrodynamic Instabilities and the Transition to Turbulence* (ed. H. Swinney & J. Gollub), pp. 181–228. Springer.

Obako, A. V. & Cassel, K. W. 2000 Large-scale and small-scale interaction in unsteady separation. *AIAA paper* 2000–2469.

Panton, R. L. 1997 *Self-sustaining Mechanisms of Wall Turbulence*. Computational Mechanics, Southampton, UK.

Peregrine, D. H. 1985 A note on the steady high-Reynolds-number flow about a circular cylinder. *J. Fluid Mech.* **157**, 493–500.

Peridier, V. J., Smith, F. T. & Walker, J. D. A. 1991*a* Vortex-induced boundary-layer separation. Part 1. The unsteady limit problem $Re \rightarrow \infty$. *J. Fluid Mech.* **232**, 99–131.

Peridier, V. J., Smith, F. T. & Walker, J. D. A. 1991*b* Vortex-induced boundary-layer separation. Part 2. Unsteady interacting boundary-layer theory. *J. Fluid Mech.* **232**, 133–165.

Robinson, S. 1991 Coherent motions in the turbulent boundary layer. *Ann. Rev. Fluid Mech.* **23**, 601–639.

Shen, J. 1991 Hopf bifurcation of the unsteady regularized driven cavity flow. *J. Comput. Phys.* **95**, 228–245.

Smith, F. T. 1985 A structure for laminar flow past a bluff body at High Reynolds number. *J. Fluid Mech.* **155**, 175–191.

Smith, C. R. & Metzler, S. P. 1983 The characteristics of low-speed streaks in the near-wall region of a turbulent boundary layer. *J. Fluid Mech.* **129**, 27–54.

Smith, C. R. & Walker, J. D. A. 1995 Turbulent wall-layer vortices. In *Fluid Vortices* (ed. S. Green), pp. 235–290. Kluwer.

Smith, C. R., Walker, J. D. A., Haidari, A. H. & Sobrun, U. 1991 On the dynamics of near-wall turbulence. *Phil. Trans. R. Soc. Lond.* A **336**, 131–175.

Stuart, J. J. 1965 *AGARD Rep.* 514.

Swearingen, J. D. & Blackwelder, R. F. 1987 The growth and breakdown of streamwise vortices in the presence of a wall. *J. Fluid Mech.* **182**, 255–290.

Thomas, A. S. W. & Bull, M. K. 1983 On the role of wall-pressure fluctuations in deterministic motions in the turbulent boundary layer. *J. Fluid Mech.* **128**, 283–322.

Tutty, O. R. & Cowley, S. J. 1986 On the stability and the numerical solution of the unsteady interactive boundary-layer equation. *J. Fluid Mech.* **168**, 431–456.

Van Dommelen, L. L. 1981 Unsteady boundary-layer separation. PhD dissertation, Cornell University.

Van Dommelen, L. L. & Shen, S. F. 1980 The spontaneous generation of the singularity in a separating boundary layer. *J. Comput. Phys.* **38**, 125–140.

Van Dommelen, L. L. & Shen, S. F. 1982 The genesis of separation. In *Proc. Symp. on Numerical and Physical Aspects of Aerodynamic Flow* (ed. T. Cebei), Long Beach, California, pp. 283–311. Springer.

Walker, J. D. A. 1990 Wall layer eruptions in turbulent flows. In *Structure of Turbulence and Drag Reduction* (ed. A. Gyr), pp. 109–118. Springer.

Walker, J. D. A., Abbott, D. E., Scharnhorst, R. K. & Weigand, G. G. 1989 Wall-layer model for velocity profile in turbulent flows. *AIAA J.* **27**, 140–149.

Walker, J. D. A. & Herzog, S. 1988 Eruption mechanisms for turbulent flows near walls. In *Transport Phenomena in Turbulent Flows* (ed. M. Hirata & N. Kasagi), pp. 145–156. Hemisphere.

Walker, J. D. A. & Scharnhorst, R. K. 1986 The Ξ function. *Report FM-9*, Department of Mechanical Engineering and Mechanics, Lehigh University.

Walker, J. D. A., Scharnhorst, R. K. & Weigand, G. G. 1986 Wall layer models for the calculation of velocity and heat transfer in turbulent boundary layers. *AIAA Paper* 86-0123.